

THE RINGED SPIRAL GALAXY NGC 4622. I. PHOTOMETRY, KINEMATICS, AND THE CASE FOR TWO STRONG LEADING OUTER SPIRAL ARMS¹

RONALD J. BUTA² AND GENE G. BYRD

Department of Physics and Astronomy, Box 870324, University of Alabama, Tuscaloosa, AL 35487

AND

TARSH FREEMAN

Bevill State Community College, Fayette, AL 35555

Received 2002 June 20; accepted 2002 October 29

ABSTRACT

The intriguing nearly face-on southern ringed spiral galaxy NGC 4622, the first galaxy definitively shown to have leading spiral structure, is revisited in this paper with new images from the *Hubble Space Telescope's* (*HST*) WFPC2, together with ground-based optical and near-IR imaging, and a Fabry-Perot $H\alpha$ velocity field. The data provide new information on the disk/bulge/halo mix, rotation curve, star formation in the galaxy, and the sense of winding of its prominent spiral arms. Previously, we suggested that the weaker, inner single arm most likely has the leading sense, based on a numerical simulation. Now, taking advantage of *HST* resolution and using de Vaucouleurs' standard extinction and reddening technique to determine the near side of the galaxy's slightly tilted disk, we come to the more surprising conclusion that *the two strong outer arms have the leading sense*. We suggest that this highly unusual configuration may be the result of a past minor merger or mild tidal encounter. Possible evidence for a minor merger is found in a short, central dust lane, although this is purely circumstantial and an unrelated interaction with a different companion could also be relevant. The leading arms may be allowed to persist because NGC 4622 is dark halo dominated (i.e., not "maximum disk" in the inner regions) and displays a significantly rising rotation curve. The new *HST* observations also reveal a rich globular cluster system in the galaxy. The mean color of these clusters is $(V-I)_0 = 1.04$, and the specific frequency is 3.4 ± 0.6 . The luminosity function of these clusters confirms the membership of NGC 4622 in the Centaurus Cluster.

Key words: galaxies: kinematics and dynamics — galaxies: photometry — galaxies: spiral — galaxies: structure

1. INTRODUCTION

The sense of winding of spiral arms in a disk galaxy is an important property that must be explained by gravitational theories of spiral structure. Although both leading and trailing waves are thought to be part of the dynamics and propagation of spiral structure, the swing amplification mechanism of Toomre (1981) demonstrates the robustness of trailing waves over leading waves. Observationally, de Vaucouleurs (1958) showed that in all spirals where it was possible to determine the sense of winding of the arms directly, the arms are trailing. De Vaucouleurs used Doppler shifts to determine which half of the major axis of a galaxy is receding from us relative to its center, and then used an asymmetry in the observed dust distribution to determine which side of the minor axis is the near side. The dust asymmetry he used is not intrinsic but is caused by the fact that, in an inclined galaxy, dust in the near side is silhouetted against the background starlight of the bulge and disk. In galaxies with significant nearly spherical bulge components this effect can be seen even if the inclination is less than 45° .

NGC 4622 is a nearly face-on southern spiral galaxy with an intriguing morphology. From a ground-based photograph, Byrd et al. (1989) pointed out that, in addition to a pair of strong, lopsided outer arms winding outward clockwise, NGC 4622 has a weaker, single inner arm winding outward counterclockwise. Byrd et al. noted that one set of arms must be leading, a very rare configuration. Buta, Crocker, & Byrd (1992, hereafter BCB) showed, using multiband surface photometry, that the single inner arm is a stellar dynamical feature, not a result of an unusual dust distribution. NGC 4622 thus became the most convincing case of a galaxy having leading spiral structure. However, these observations could not determine which set of arms is leading. Based on theory and numerical simulations, Byrd, Freeman, & Howard (1993) suggested that the inner arm leads.

We present new *Hubble Space Telescope* WFPC2 images of NGC 4622 that challenge this conclusion. These images, together with a ground based Fabry-Perot $H\alpha$ velocity field, give the surprising and completely unexpected result that the two outer arms in NGC 4622 must be leading. The images also reveal (circumstantial) evidence for a past merger between NGC 4622 and a smaller galaxy. These results challenge current theories of spiral structure in galaxies and suggest that strong two-armed leading spirals can result from an interaction.

The new observations are summarized in § 2. In § 3 we discuss the morphology and group membership of NGC 4622, and consider its distance, which is important for the analysis

¹ Based on observations with the NASA/ESA *Hubble Space Telescope*, obtained at the Space Telescope Science Institute, which is operated by the Association of Universities for Research in Astronomy, Inc., under contract NAS 5-26555.

² Visiting Astronomer, Cerro Tololo Inter-American Observatory, which is operated by AURA, under cooperative agreement with the National Science Foundation.

in this paper. In § 4 we discuss the results of surface photometry and bulge, disk, and Fourier decomposition. Section 5 covers the velocity field and rotation of the galaxy, while § 6 discusses the sense of winding of the spiral arms. Section 7 presents models that show how we can detect a near side–far side reddening and extinction asymmetry, to inclinations as low as 15° , at *HST* resolution. Sections 8 and 9 analyze the globular clusters and associations in the galaxy. A discussion is presented in § 10, and conclusions follow in § 11.

2. OBSERVATIONS

2.1. Hubble Space Telescope Optical Imaging

The *HST* observations of NGC 4622 were secured on 2001 May 25 with WFPC2. The center of the galaxy was placed within the WF3 and positioned such that the whole galaxy lies within the WFPC2 field. For most of the galaxy, the pixel size on these images is $0''.1$, or 19.5 pc at the adopted distance of 40.2 Mpc (see § 3). The WF2/WF3 and WF3/WF4 boundaries cover $160''$, or 31 kpc at the adopted distance. Four broadband filters were used to observe the galaxy: F336W, F439W, F555W, and F814W. These four filters approximate the Johnson *U*, *B*, *V*, and Cousins *I* photometric systems, respectively.

The total exposure times were 2000 s each for F336W and F439W, and 1000 s each for F555W and F814W. The observations were made in a CRSPLIT mode to facilitate removal of cosmic rays. After receiving the standard pipeline preprocessed images, the separate images were corrected for bad pixels and columns, using IRAF³ STSDAS routine WFIXUP, and then the images for each filter were combined, using STSDAS routine CRREJ. The latter routine was very effective at removing most of the cosmic rays. The gain used was $7 e^- \text{ADU}^{-1}$ and the read noise was $5.2 e^-$.

2.2. Ground-based Optical and Near-Infrared Imaging

Optical images of NGC 4622 in *B*- and *I*-band filters were obtained on 1992 March 30 UT with the 1.5 m telescope of the Cerro Tololo Inter-American Observatory (CTIO). A Tek2 1024 × 1024 CCD was used with a gain of $1.6 e^- \text{ADU}^{-1}$ and a read noise of $4 \pm 1 e^-$. The scale of these images is $0''.435 \text{ pixel}^{-1}$, or 84.8 pc at the adopted distance. Exposure times were 600 s in *B* and 300 s in *I*. The observations were bias-corrected, flat-fielded, and cosmic-ray-cleaned using standard IRAF routines.

Near-infrared Johnson *H*-band observations of NGC 4622 were obtained on 1996 February 9 UT with the CTIO Infrared Imager (CIRIM) attached to the 1.5 m telescope. CIRIM was used with a gain of $9 e^- \text{ADU}^{-1}$ and a read noise of $37 e^-$. The procedures outlined by Joyce (1992) were followed on both the acquisition and reduction of these observations. The scale of these observations is $1''.137 \text{ pixel}^{-1}$ (221.6 pc), and a total exposure time of 900 s was achieved.

2.3. Ground-based $H\alpha$ Fabry-Perot Interferometry

Observations at $H\alpha$ with the Rutgers Fabry-Perot Interferometer (RFP) on the CTIO 4 m telescope were obtained

by R. J. B. and G. B. Purcell on 1992 March 29 UT. Eleven frames separated by about 1 Å were needed, covering a velocity range of 500 km s^{-1} . The reduction of these images used standard IRAF tasks and IRAF-based routines, and the procedure is described by Purcell (1998) and Buta & Purcell (1998). A preliminary reduction and analysis of the velocity field was presented by Scott (1996). We have used revised routines from Purcell (1998) to rereduce the velocity field and improve its quality.

To match the coordinate systems of the WFPC2, Tek2, CIRIM, and RFP images, we used an image from the Digitized Sky Survey and STSDAS task XYEQ to measure accurate coordinates of field stars around NGC 4622. This analysis provided accurate checks of the scales and the relative orientations of the images. The analysis also led to the identification of a bright supernova (SN 2001jx) that was present at the time of the WFPC2 observations. Information on astrometry and photometry of the supernova is provided in Appendix B.

3. MORPHOLOGY, GROUP MEMBERSHIP, AND DISTANCE

Figure 1 shows a color image based on the four WFPC2 images of NGC 4622. These images include only the part of the WFPC2 field occupied by the galaxy and exclude some of the surrounding field. The color image captures all of the salient features of the galaxy. Recent star formation is confined mainly to the two outer arms and the southwest portion of the inner ring (see also Fig. 1 of BCB). The weaker, single inner arm can be traced for more than 540° , and it only has recent star formation near its juncture with the east outer arm. The faint, yellow starlike objects scattered across the central area are globular clusters (see § 8). These stand out in color fairly well from faint red foreground stars and background galaxies. The color image also shows thin dust lanes at the juncture between the inner single arm and the west outer arm. This is the first time clear dust lanes have been identified in NGC 4622.

The central region of NGC 4622 shows a previously unknown feature in the new WFPC2 images: a central dust lane. This is shown for the *V* band and in the *V*–*I* color index in Figure 2. The feature is well defined and almost splits the nucleus into equal halves. Detailed *HST* studies of the central regions of spiral galaxies in both optical (Carollo, Stiavelli, & Mack 1998) and near-IR (Carollo et al. 2002) filters reveal a wide variety of nuclear morphological features, but nucleus-splitting dust lanes in nearly face-on early-type spiral galaxies appear to be rare. The presence of such a feature in NGC 4622 suggests that the galaxy has suffered from a minor merger that may have destroyed a small companion. The central dust lane does not extend much outside the nucleus and is sharper than most of the other dust features seen in the WFPC2 images. The feature is most reminiscent of the striking “X-shaped” dust lane crossing the nucleus of M51 (Grillmair et al. 1997). At least one “arm” of this feature has been suggested to be an edge-on accretion disk feeding the central AGN in M51. However, the feature in M51 is clearly more complex than that in NGC 4622, and Grillmair et al. argue that the dust lane obscuring the center of M51 is too asymmetric to be part of a disk. More properties of the central dust lane in NGC 4622 are given in § 4.3.

³ IRAF is distributed by the National Optical Astronomy Observatory, which is operated by AURA, under cooperative agreement with the NSF.



FIG. 1.—Hubble Heritage color image based on the F336W, F439W, F555W, and F814W WFPC2 images of NGC 4622. In this and all other WFPC2 images in this article, north is oriented 30° clockwise from the top vertical, while east is oriented 30° clockwise from the left horizontal. The field shown is $1'.57 \times 1'.38$.

NGC 4622 has been assigned to Lyon Galaxy Group (LGG) number 305 (Garcia 1993). From the database available at the time, 16 galaxies could be assigned to this group, whose mean luminosity-weighted heliocentric radial velocity is 4351 km s^{-1} . However, two other groups are in the same general area: LGG 298, which has 54 members at a mean radial velocity of 2900 km s^{-1} , and LGG 301, which has eight members at a mean radial velocity of 2294 km s^{-1} ,

indicating a possible superposition of unrelated groups. However, this is not the case. The nature of this puzzling situation was actually clarified earlier by Lucey, Currie, & Dickens (1986), who found a bimodal velocity distribution in Centaurus. These authors suggested that although the two velocity components are separated by about 1500 km s^{-1} (with one component at a mean radial velocity of 3000 km s^{-1} [Cen30] and the other component at 4500 km s^{-1}

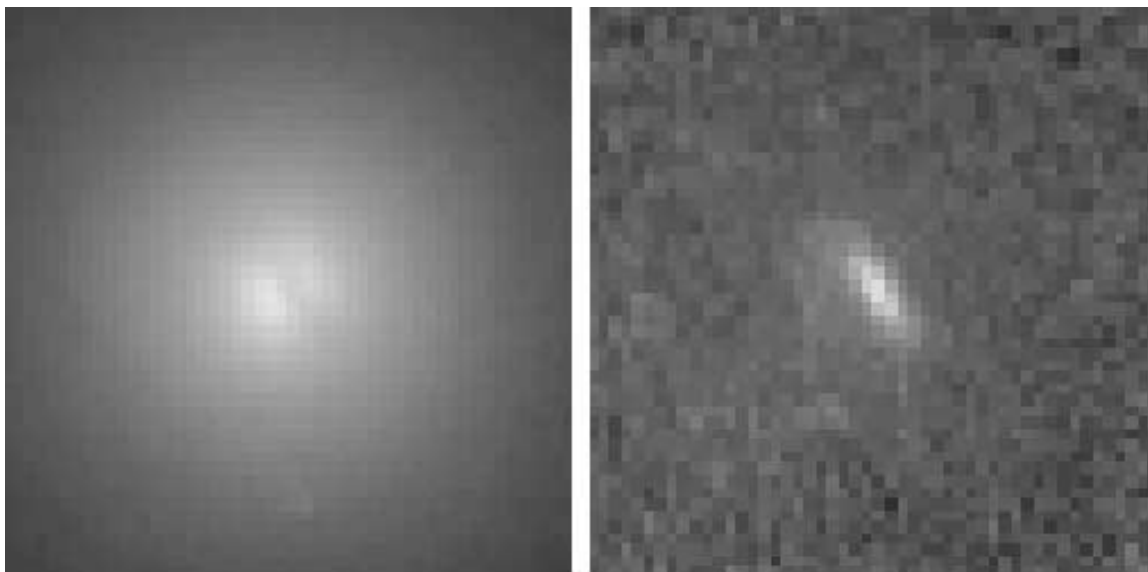


FIG. 2.—The central $5'' \times 5''$ of NGC 4622 in the V -band (F555W) image (*left*) and in $V-I$ (*right*), showing the strong central dust lane. North is to the upper right, and east to the upper left, as in Fig. 1. The color index map is coded such that redder features are light and bluer features are dark.

[Cen45]), analysis of the color-magnitude relation for the E galaxies in each group suggested a similar distance. NGC 4622 is close to NGC 4616, an E galaxy with a similar redshift (see Fig. 3 of BCB). Both are part of Lucey et al's subgroup called "WBCen45," meaning they are in an elongated feature called the "western branch." Lucey et al. suggested that there was a possibility that members of WBCen45 were part of a background group whose mean redshift is 4770 km s^{-1} , based on the smaller sizes of the spirals compared with those in WBCen30. However, this was not clear cut, and most of Cen45, including the main elliptical NGC 4709, was considered to be part of the same cluster as Cen30 (corresponding to LGG 298) but undergoing an infall, rather than being a separate group in the background.

Tully & Pierce (2000) have recently determined the distance to Cen30 using the Tully-Fisher relation. From 13 galaxies and a revised calibration of the relation, they obtained a distance modulus of 33.02 ± 0.17 , corresponding to a distance of 40.2 ± 3.1 Mpc. The rms scatter about their template relation was 0.60 mag, the largest of the 12 clusters studied. A recent study of distances from the surface brightness fluctuation (SBF) method (Tonry et al. 2001) suggests that WBCen45 may not be simply background galaxies. Two members of LGG 305 (NGC 4616 and NGC 4709) and a third likely member (ESO 323-34) are in the SBF database (Table 1 of Tonry et al. 2001) and have an unweighted mean distance modulus of 32.80 ± 0.16 (s.d.), corresponding to a distance of 36.3 ± 2.7 Mpc. The mean radial velocity (4787 km s^{-1}) of these galaxies relative to the cosmic microwave background radiation is the same as that for NGC 4622 (4779 km s^{-1}), and their mean distance modulus agrees within uncertainties with that for Cen30.

NGC 4616 and NGC 4603D, the two large galaxies closest to NGC 4622 in Figure 3 of BCB, have apparent B_T magnitudes of 14.4 and 14.1, respectively, compared with 13.4 for NGC 4622. If both NGC 4616 and NGC 4603D are bona fide members of the Centaurus Cluster, then NGC 4622 is very likely also a member and not part of the back-

ground group discussed by Lucey et al. (1986). We therefore adopt 40.2 Mpc as the best estimate of the distance to NGC 4622. This is supported by our analysis of the luminosity function of the globular clusters in § 8.

4. SURFACE PHOTOMETRY

Surface photometry provides a way of connecting the ground-based and space-based observations. First we analyze the ground-based optical and near-IR images to reevaluate the photometric orientation parameters of the galaxy and to assess bulge and disk properties. Sky background levels on the optical and near-IR images were estimated, using IRAF routine IMSURFIT, by fitting a plane to background intensities in a surrounding border after removal of foreground stars and other field objects. In both sets of images the field of view was large enough to insure accurate sky subtraction. For the WFPC2 images, we used IRAF routine FITSKY to estimate the average background in sections of the WF2 and WF4 fields farthest from the center of the galaxy. Although the galaxy clearly fills the entire WFPC2 field, this approach is adequate because, for profile modeling purposes, we use the ground-based images exclusively at the lowest surface brightness levels and the WFPC2 images at the highest surface brightness levels.

4.1. *Isophotal Ellipse Fits*

The CTIO B - and I -band images are the deepest images we have obtained of NGC 4622. The B -band image is displayed in Figure 3 to show faint outer isophotes. These become rather round at large radii. To reevaluate the orientation parameters, we first cleaned the images of foreground stars and field galaxies, using a combination of point-spread function (PSF) fitting and image editing. IRAF routines ALLSTAR and IMEDIT were used for this purpose. The cleaned images were then block-averaged in 8×8 pixel boxes and ellipses were fitted to isophotes in steps of $0.1 \text{ mag arcsec}^{-2}$. Figure 4 shows how the axis ratio and posi-

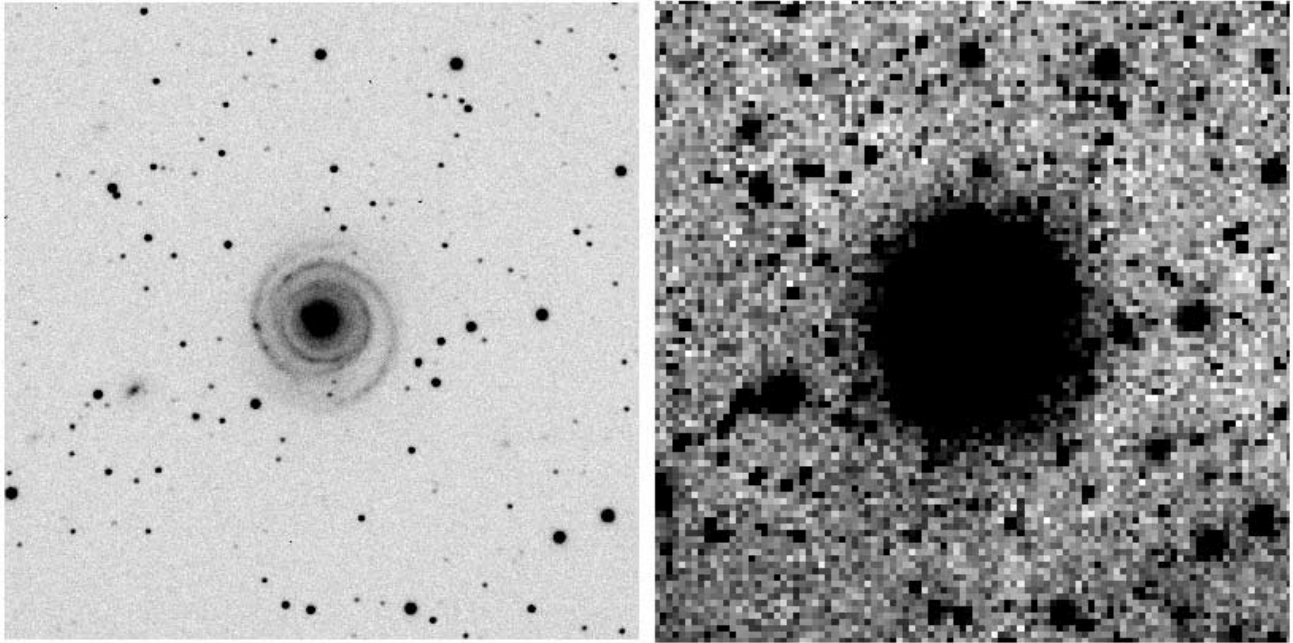


FIG. 3.—*Left*: B-band image of NGC 4622 obtained with the CTIO 1.5 m telescope. *Right*: the same image block-averaged 8×8 pixels and displayed to reveal the very faint outer isophotes. Each field is $5'0$ square. In this and all other ground-based images in this article, north is to the top, and east to the left.

tion angle of the fitted ellipses vary in the outer parts of the galaxy. For these fits, 2σ rejection was used for isophotes fainter than $26.0 \text{ mag arcsec}^{-2}$. The position angles of the outer isophotes become fairly constant beyond $a = 55''$. Restricting to $55'' \leq a \leq 85''$, the mean axis ratio is 0.903 ± 0.030 and the mean position angle is $-13^\circ.1 \pm 8^\circ.4$

(or $166^\circ.9 \pm 8^\circ.4$). For an oblate spheroid with an intrinsic axis ratio of 0.2 (see Schommer et al. 1993; Tully & Pierce 2000), the mean axis ratio implies an inclination of $26^\circ \pm 4^\circ$. However, the mean photometric major-axis position angle is offset 35° from the line of nodes for circular rotation (§ 5). An intrinsic distortion in the outer parts of the disk may be responsible for this offset.

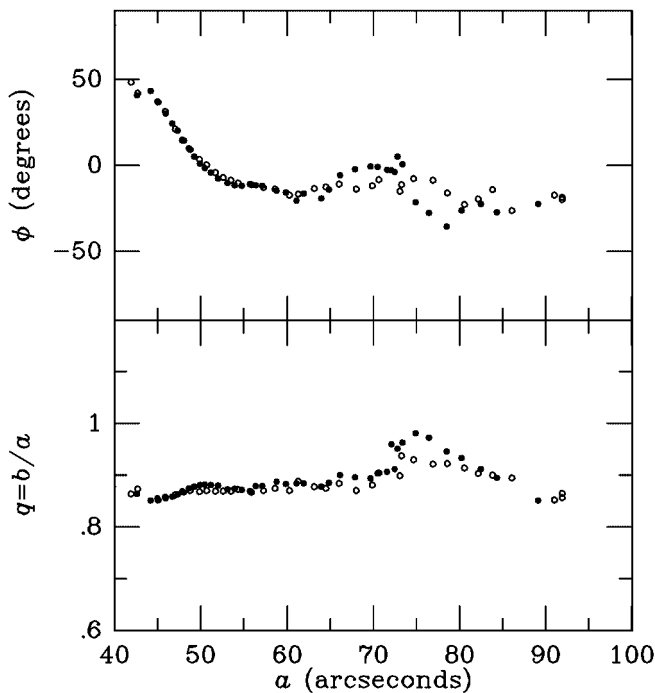


FIG. 4.—Plots of minor-to-major axis ratio q and position angle ϕ vs. semimajor-axis radius a of low-resolution outer isophotes of NGC 4622, based on ellipse fits. Filled circles are for B , while open circles are for I . The position angle ϕ is measured eastward from north.

4.2. Decomposition of Major- and Minor-Axis Luminosity Profiles

Analysis of the velocity field in § 5 shows that the kinematic line of nodes of NGC 4622 is in position angle $+22^\circ$. Figure 5 shows mean (folded) luminosity profiles along this position angle and the implied kinematic minor-axis position angle. Plots of the profiles versus $r^{1/4}$ show that the bulge can be approximated by an $r^{1/4}$ law over the range $2''.5 \leq r \leq 11''.7$. The outer parts of the profiles display an exponential decline in surface brightness outside the bright spiral arms. Thus, we have carried out a standard bulge/disk decomposition by fitting a combination of the following equations to limited ranges of the profiles:

$$\mu^{\text{I}} = a^{\text{I}} + b^{\text{I}} r^{1/4}, \quad (1a)$$

$$\mu^{\text{II}} = a^{\text{II}} + b^{\text{II}} r, \quad (1b)$$

where the superscript I refers to the bulge and the superscript II refers to the disk. Although a more generalized law for the bulge, such as a Sérsic (1968) law with variable bulge exponent (Mollenhoff & Heidt 2001), might provide a better description of the bulge profile (see, e.g., § 4.3), we have used the de Vaucouleurs $r^{1/4}$ law as an approximation in order to take advantage of the Young (1976) asymptotic volume density for the $r^{1/4}$ law for the purposes of modeling the near side–far side reddening asymmetry (see § 7 and Appendix A).

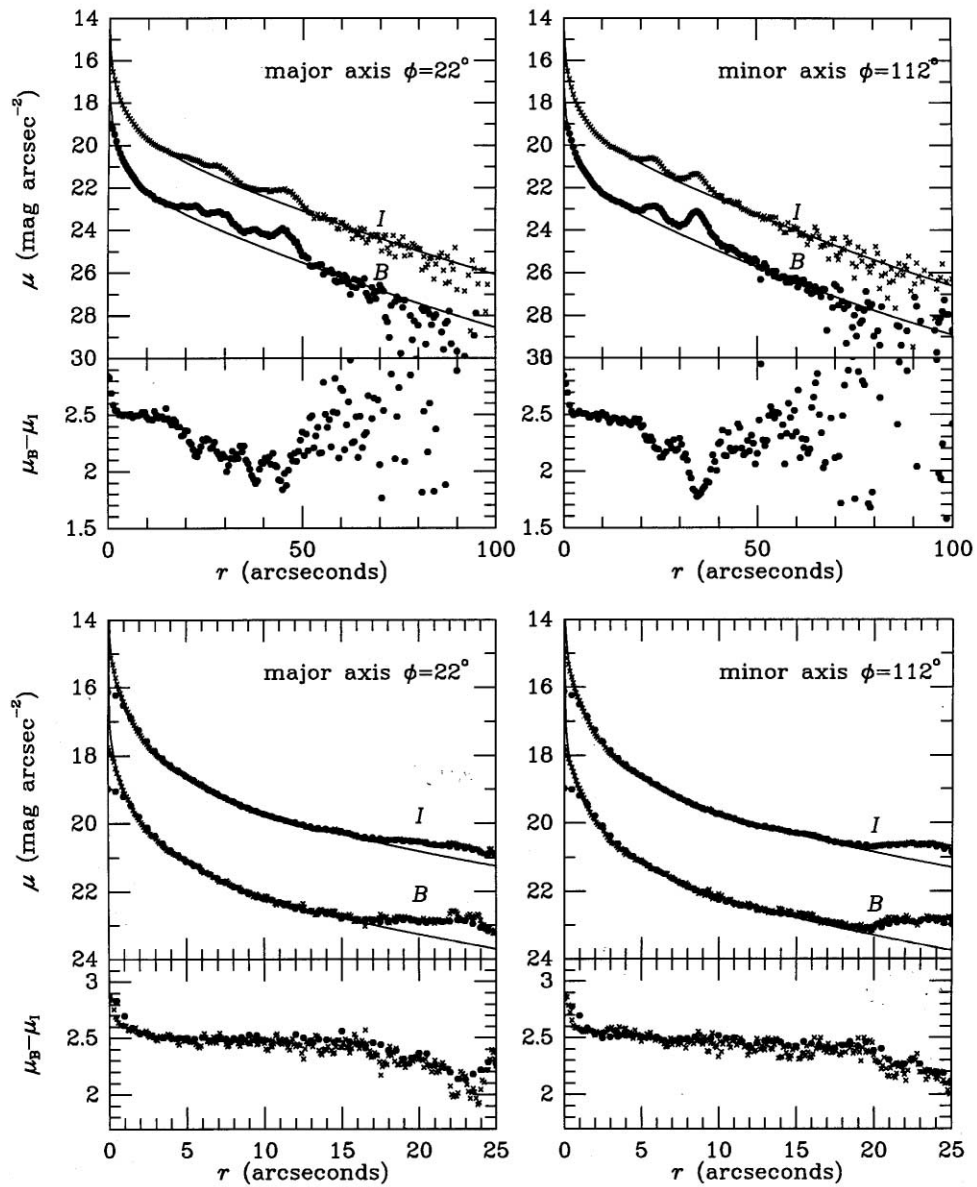


FIG. 5.—Folded major- and minor-axis profiles of NGC 4622, showing the combined bulge and disk model in B and I . In the lower panels, filled circles refer to ground-based data, while crosses refer to WFPC2 data.

For B and I , only points in the ranges $2''.5$ – $16''.0$ and $53''.0$ – $60''.0$ were used for the major-axis fits, and $2''.5$ – $16''.0$ and $53''.0$ – $65''.0$ for the minor-axis fits. These ranges avoid the humps due to the bright spiral arms. Inside $2''.5$, the light distribution departs from the $r^{1/4}$ law (see next section). We used composite profiles for these fits, using the *HST* data from $2''.5$ – $6''.0$, and the ground-based profiles for all larger radii. Table 1 summarizes the results of the fits for the parameters a^I , b^I , a^{II} , and b^{II} . The combined solutions are plotted as solid curves in Figure 5, while the separate solutions are plotted on the low-resolution ground-based major-axis profiles in Figure 6. Since the isophotes of the bulge are round, the scatter in the parameter b^I reflects mainly fitting uncertainties. The models do not reveal a significant difference in bulge effective radius between the B and I filters; therefore we adopt an average slope $\langle b^I \rangle = 4.7585 \pm 0.0652$, corresponding to an effective radius $r_e^I = 9''.38 \pm 0''.56$ or 1.83 ± 0.11 kpc.

For the H -band decomposition, we could not derive a reliable bulge model directly, given the low resolution. Instead, we forced the slope b^I to be 4.7585 and solved for the other three parameters in equations (1a) and (1b). Table 1 summarizes these parameters for both the major and

TABLE 1
BULGE/DISK SOLUTIONS FOR NGC 4622

Profile	a^I	b^I	a^{II}	b^{II}
Major-axis B	14.3375	4.7239	22.3846	0.06963
Major-axis I	11.9377	4.6395	19.9959	0.07070
Major-axis H	9.6429	(4.7585)	18.1477	0.07330
Minor-axis B	14.4436	4.7261	22.2001	0.07837
Minor-axis I	11.5837	4.9445	19.7284	0.07808
Minor-axis H	9.7237	(4.7585)	17.9286	0.07945

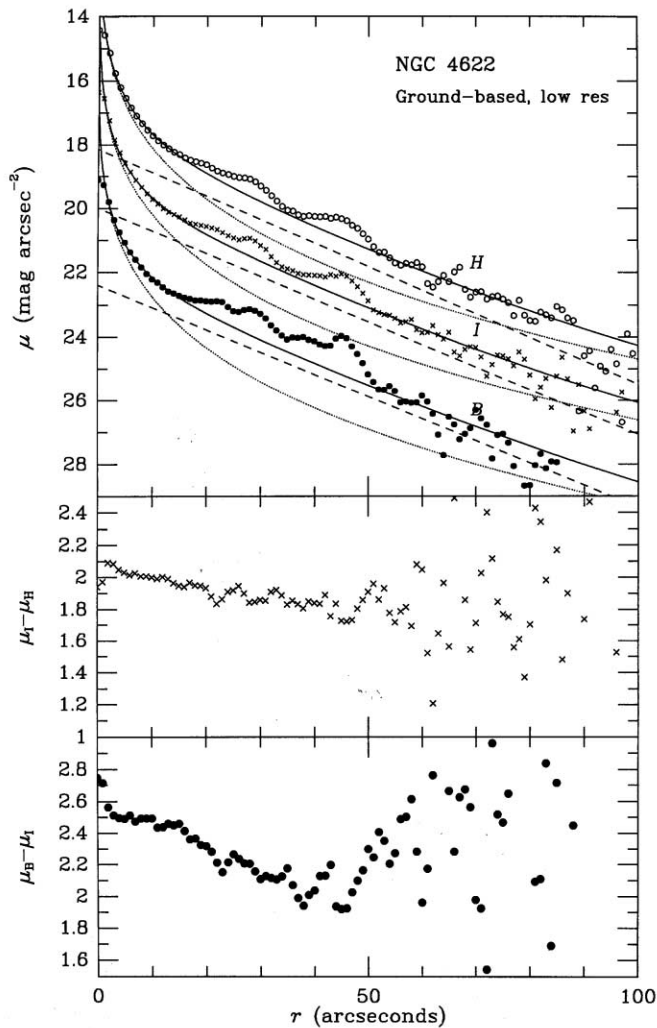


FIG. 6.—Folded major-axis profiles of NGC 4622 in the H -band and in B and I matched to the resolution of the H -band image. Bulge, disk, and total profiles are shown based on standard decompositions.

minor axes, and Figure 6 shows the solutions for the major axis. For the fits, we used points in the range $3''.0$ – $16''.0$ and $53''.0$ – $85''.0$ for the major axis, and $3''.0$ – $16''.0$ and $45''.0$ – $65''.0$ for the minor axis.

The parameters in Table 1 for the slope $\langle b^{\text{II}} \rangle$ are also not significantly different between B and I along each axis. The averages yield a major-axis effective radius $a_e^{\text{II}} = 25''.97$ and a minor axis effective radius of $b_e^{\text{II}} = 23''.30$. The axis ratio, $b_e/a_e = 0.897$, is consistent with an inclination of 26° . The mean B -band central surface brightness $\langle a^{\text{II}} \rangle = 22.29 \pm 0.09$ corresponds (for Galactic extinction $A_B = 0.598$ mag, Schlegel, Finkbeiner, & Davis 1998, and an inclination of 26°) to a corrected value $B(0)_c = 21.81$ mag arcsec $^{-2}$, within the original range of this parameter noted by Freeman (1970).

The parameters from this decomposition for B and I agree well with those derived by BCB. From purely ground-based profiles based on TI CCD images, the average bulge effective radius from B and I filters was $8''.8 \pm 0''.4$, while the average disk major-axis effective radius was $28''.5 \pm 0''.9$.

The decompositions indicate that the bulge is a significant contribution to the total luminosity of NGC 4622. To determine the relative flux contribution of the bulge, we com-

puted total magnitudes in B , I , and H by extrapolating the bulge/disk decomposition profiles. This led to $B_T = 13.44$ and $I_T = 11.09$, to be compared with 13.37 and 11.13, respectively, derived by BCB. The total H -band magnitude was found to be $H_T = 9.16$. Using the mean values of a^{I} in all three filters, an effective radius of $9''.38$, and the revised total magnitudes derived here, we find that the bulge of NGC 4622 contributes 39%, 51%, and 58% of the B -, I -, and H -band luminosities, respectively. The B -band value is consistent with a Hubble type of Sa, according to Table 3B of Simien & de Vaucouleurs (1986). The other photometric parameters are consistent with this same Hubble type, based on Figures 4 and 6 of Simien & de Vaucouleurs (1986). Thus, in spite of the apparent asymmetries, NGC 4622 has normal parameters for its type.

For the adopted distance of 40.2 Mpc, NGC 4622 has a total absolute magnitude of $M_B^{b,k,i} = -20.3$. This would make it an intermediate-luminosity Sa spiral.

4.3. The Central Light Distribution and Dust Lane

The $r^{1/4}$ law does not describe the central light distribution of NGC 4622. There is excess light over the $r^{1/4}$ law defined by the outer parts of the bulge in this region. This excess was evident even in the ground-based study of BCB, where the residual I -band light distribution showed a small ring of excess light around the center. A better representation of the light distribution in this region is provided by a “Nuker” law, which describes the central regions of many ellipticals (Lauer et al. 1995; Faber et al. 1997). The Nuker law includes the parameters α , β , and γ , which define its shape, and two other parameters, μ_b and r_b , which describe the surface brightness and radius of the “break” point on the profile. For ellipticals, if the parameter $\gamma < 0.3$, the galaxy is a “core type,” while, if $\gamma > 0.3$, the galaxy is a “power-law” type.

The central light profile in NGC 4622 was derived by fitting free ellipses to the central two-dimensional light distribution, using the STSDAS routine ELLIPSE (Jedrezewski 1987). These profiles are shown for B , V , I , $B-V$, and $V-I$ in Figure 7. The central dust lane impacts these profiles and causes the small dips in the B and V profiles and the small peaks in $B-V$ and $V-I$. The I -band profile is least affected, so we fit only this profile for the Nuker law parameters. Excluding points having $\log r > 2.575$ ($r > 376$ pc), we derive $\alpha = 2.188 \pm 0.086$, $\beta = 1.208 \pm 0.010$, $\gamma = 0.059 \pm 0.019$, $\mu_b(I) = 15.016 \pm 0.010$, and $r_b = 67.88 \pm 0.97$ pc. Thus, the central profile is a “core” type. In ellipticals core types are characteristic of the more massive and luminous cases. Kormendy (1987) reviews many of the known properties of cores in E galaxies and bulges.

Figure 7 also shows the ellipticity ϵ and position angle ϕ of the fitted ellipses near the center. Beyond $r = 125$ pc [$\log(r) = 2.1$] the ellipticity is below 0.05.

The properties of the central dust lane were derived by fitting ellipses to isochromes in the central $1''$ radius. The IRAF routine ELLIPSE was also used for this purpose. Figure 8 shows the axis ratio and position angle of the fitted ellipses as a function of radius. The isochromes have a nearly constant axis ratio of $\langle q \rangle = 0.38 \pm 0.01$ from $0''.15 \leq a \leq 0''.70$. Out to its apparent edge the diameter of the feature is $1''.4 = 273$ pc, while its width along its minor axis is $0''.53$, or 104 pc. Figure 8 shows that, over the same radius range, the position angle increases from 60° to about

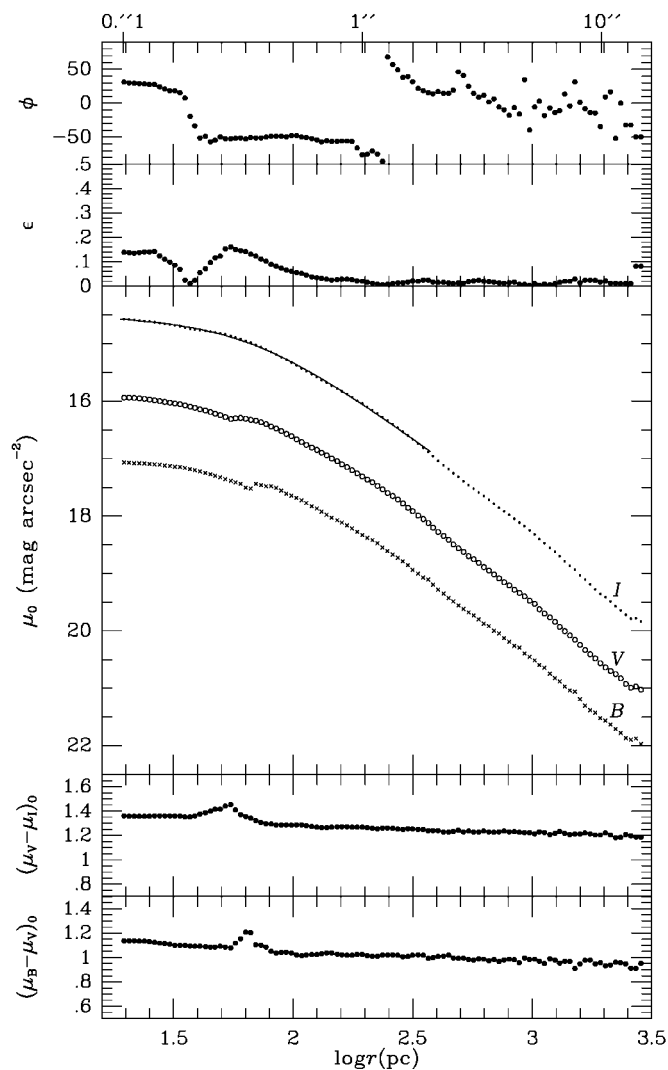


FIG. 7.—Ellipse fit surface brightness and color indices (both corrected for Galactic extinction), ellipticity ϵ , and position-angle (ϕ) profiles within $r = 16''$. The solid curve superposed on the I -band profile is a fit of a Nuker law to the central surface brightnesses. The position angle ϕ is measured eastward from north, and the radius scale in parsecs is based on a distance of 40.2 Mpc.

65° , a possible signature that the dust lane represents an edge-on, slightly warped central dust disk. Although ionized gas was not detected in this region in the ground-based $H\alpha$ Fabry-Perot interferometry, high-resolution $H\alpha$ observations might verify this possibility.

4.4. Fourier Decomposition

Fourier decomposition provides another useful way of dissecting the structure of NGC 4622. It was used by BCB to analyze their ground-based images, and we repeat their analysis here using the WFPC2 data. We investigate the Fourier structure of the stellar background in the I -band WFPC2 image, as well as the variation of relative Fourier amplitudes and phases with radius in B , V , and I .

Figure 9 shows four images that duplicate those shown by BCB but are at higher resolution. The figure shows the $m = 0, 1$, and 2 Fourier components, in addition to an image that sums the $m = 0-6$ components, based on a routine that

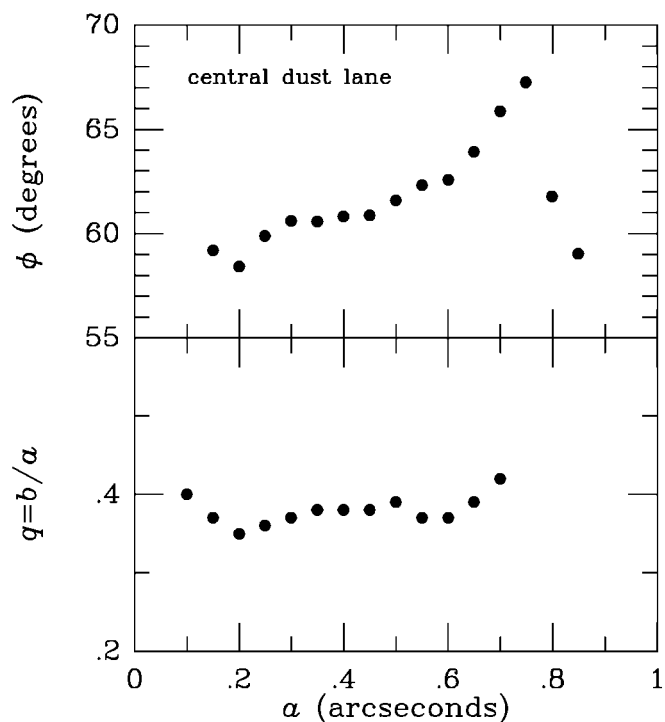


FIG. 8.—Results of ellipse fits to isochromes of the central dust lane. The isochromes fitted range from $V-I = 1.45-1.72$. The parameter q is the minor-to-major axis ratio. The position angle ϕ is measured eastward from north.

computes circular averages centered on the nucleus. The $m = 1$ image shows a complete inner spiral arm, which clearly winds at least 540° and which is distinct from all the other structure in the map. The map also shows that there is some asymmetry within the bright bulge region, especially south of the center. The $m = 2$ map reveals the two bright outer arms and little structure in the region dominated by the single inner arm. The $m = 0$ image is dominated by a ring that represents the average feature seen.

The $m = 0-6$ image provides a very good approximation to the total stellar background, and we show in Figure 10 the difference between the full mosaic I -band image and this summed Fourier image. The figure highlights the smallest-scale structures and so provides an intriguing map of the distribution of star clusters, both young and old, in NGC 4622. The map also reveals lanes of dust on the west and south sides of the inner ring, but it is surprisingly less sensitive to the dusty structures evident to the east in the original *HST* image.

Figures 11a and 11b show the relative amplitudes and phases of the $m = 1$ and $m = 2$ Fourier components. These are higher resolution versions of Figure 9 of BCB, but, unlike BCB, the amplitudes and phases are now based on deprojected images using the inclination and line of nodes derived in § 5. Both Fourier components show relative amplitudes generally less than 10% inside $r = 16''$. Figure 11a shows once again the interesting phase change in the $m = 1$ component from B to V to I in the vicinity of the inner ring ($21''.5 \leq r \leq 28''.5$). The possible significance of this change was discussed by BCB and Byrd et al. (1993). We consider it again here in § 10.4, as well as other details in the plots.

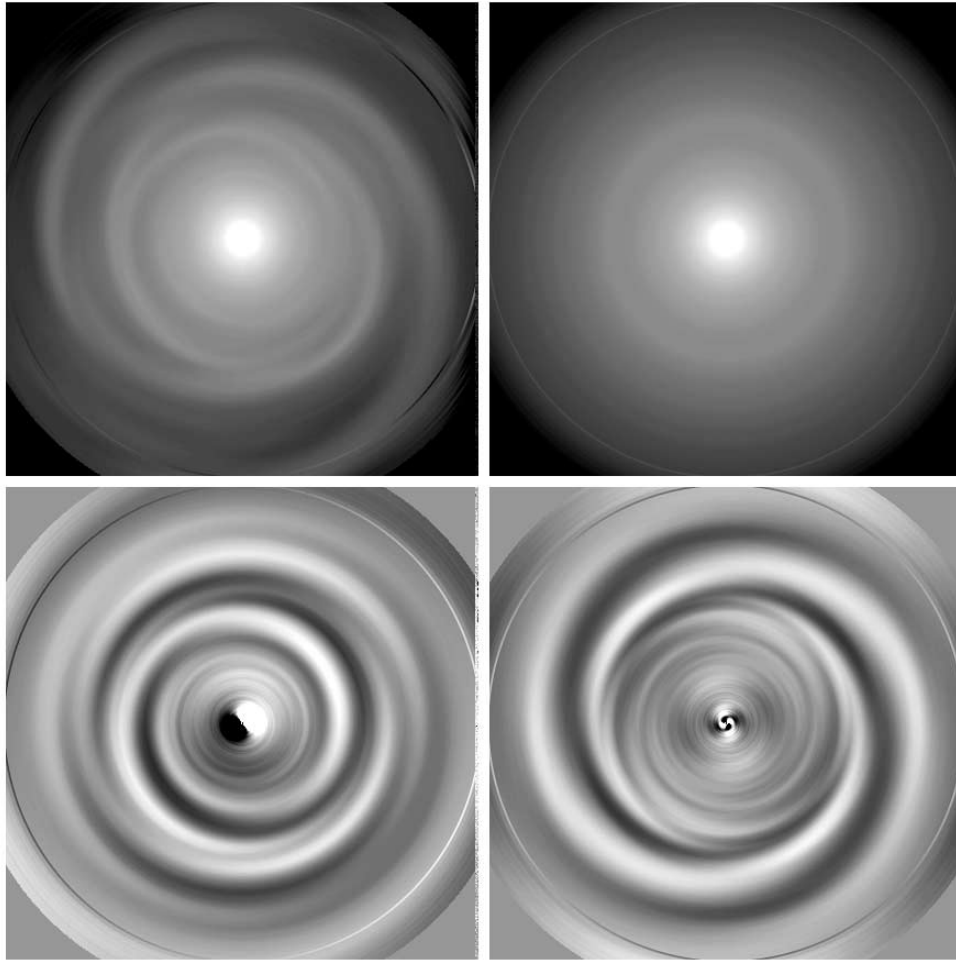


FIG. 9.—Fourier decomposition (sky plane) of the WFPC2 *I*-band stellar background light distribution of NGC 4622. *Top left*: Sum of $m = 0$ –6 terms. *Top right*: $m = 0$ image. *Bottom left*: $m = 1$ image. *Bottom right*: $m = 2$ image. North is to the upper right, and east to the upper left, as in Fig. 1. Each frame covers a field of $1'.50 \times 1'.43$.

5. VELOCITY FIELD AND ROTATION

5.1. Dynamical Parameters and Rotation Curve

Critical to our interpretation of NGC 4622 is the velocity field and the rotation of the disk. Figure 12 shows the continuum and emission maps from the $H\alpha$ Fabry-Perot interferometry. The emission map shows that the $H\text{ II}$ regions in NGC 4622 lie mainly along the two main outer arms and the southwest half of the inner ring. Little or no $H\alpha$ emission is detected inside the inner ring. The $H\alpha$ distribution is asymmetric with stronger emission in the east outer arm, as opposed to the west outer arm.

The velocity field of NGC 4622 is shown in Figure 13. In spite of the low apparent inclination, NGC 4622 shows a well-defined line of nodes, the velocity gradient being along the northeast/southwest direction, consistent with the orientations of isophotes just outside the main spiral arms. The Fabry-Perot analysis also provided information on velocity dispersions within the ionized gas disk. However, the map (not shown here) only displays an irregular distribution of small dispersions (less than 20 km s^{-1} in general), and only a few small isolated patches having up to 50 km s^{-1} dispersion. There is no pattern to suggest any serious disruption of the velocity field perpendicular to the main disk plane.

The kinematic parameters of NGC 4622 were derived assuming only circular motions are present and using the iterative method of Warner, Wright, & Baldwin (1973). All velocity points were used, weighted according to the cosine of the angle of each point relative to the line of nodes in the galaxy plane. The lack of significant ionized gas inside the inner ring made it difficult to solve for the rotation center; thus, we forced the rotation center in this analysis to be coincident with the red continuum optical center. This method also did not constrain the inclination reliably, with any inclination between 10° and 30° being possible. This is not unusual for a low-inclination galaxy. Thus, we have used a different approach to estimate the kinematic value of this parameter.

The method we use to infer a kinematic inclination is the Tully-Fisher relation in conjunction with an observed 21 cm line width. At the time of this writing, we were unable to find a published 21 cm line profile and width, but were able to have the galaxy observed at $H\text{ I}$ specially with the Parkes 64 m telescope. This spectrum, obtained by M. Meyer (2002, private communication), will be presented elsewhere. The main result is that NGC 4622 shows an asymmetric double-horned line profile having a line center corresponding to an (optically defined) systemic velocity of $4502 \pm 3 \text{ km s}^{-1}$ and

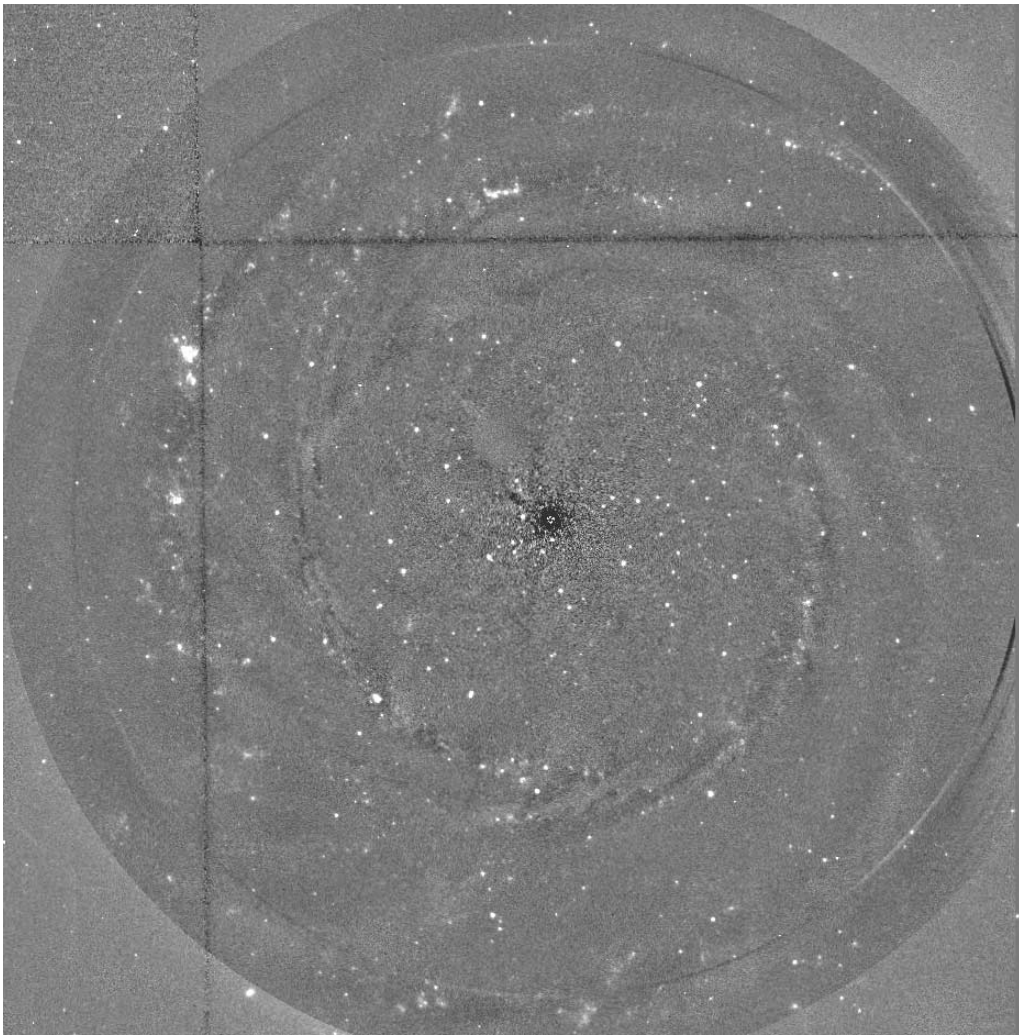


FIG. 10.—*I*-band WFPC2 image of NGC 4622 after subtraction of the $m = 0-6$ Fourier components. This removes the bulge, disk, and smooth background light of the spiral arms to reveal mostly the young and old cluster systems in NGC 4622. Orientation of this image is the same as for Fig. 1. The field shown is $1'.54 \times 1'.58$.

a line width $W_{20} = 157 \pm 5 \text{ km s}^{-1}$. We ask what the inclination of NGC 4622 would have to be to give a distance in the range $40.2 \pm 3.1 \text{ Mpc}$. We use the *I*-band total magnitude (11.09) derived in this paper and the corrections for inclination, *K*-dimming, and Galactic extinction as described by Tully & Pierce (2000). With equation (7) of Tully & Pierce (2000) and the newly measured 21 cm line width, we obtain a distance to NGC 4622 in the range $40.2 \pm 3.1 \text{ Mpc}$ for an inclination in the range 19.3 ± 1.7 , excluding uncertainties in the total magnitude. The expected maximum rotation velocity would be $190 \pm 16 \text{ km s}^{-1}$. Additional uncertainties inherent in using this method include the reliability of using a relation defined entirely by galaxies more inclined than 45° , and the complexities of the Centaurus Cluster itself. Nevertheless, the 21 cm line width analysis suggests that NGC 4622 is less inclined than the value of 26° , which was derived from the isophote fitting method.

With an inclination of 19° and a rotation center coincident with the nucleus, iteration for the remaining parameters gave a heliocentric systemic radial velocity of $4502 \pm 3 \text{ km s}^{-1}$ and a kinematic line of nodes position angle of $22^\circ \pm 5^\circ$ (J2000.0). The systemic velocity is in excellent

agreement with the 21 cm value. However, the position angle differs by 35° from the mean photometric major-axis position angle derived in § 4.1, probably because of the low inclination. The systemic velocity is larger by more than 100 km s^{-1} than the value given in RC3 (de Vaucouleurs et al. 1991).

Figure 14 shows the implied rotation curve of NGC 4622 on each side of the minor axis, while Table 2 summarizes the folded mean rotation curve. The error bars shown are standard deviations σ around the means after two cycles of 2σ rejection. On each side the rotation velocity appears to rise with radius. On the northeast side the rise is linear and almost solid body. On the southwest side (the side with the most apparent asymmetry) the rise is more gentle followed by a rapid change, with the last point reaching 300 km s^{-1} . This is much higher than the expected maximum rotation velocity from the 21 cm line width.

5.2. Constant Mass-to-Light Ratio Analysis

To evaluate the meaning of the observed rotation curve, we have used the *H*-band light distribution to compute the gravitational potential due to the stars in NGC 4622. Since

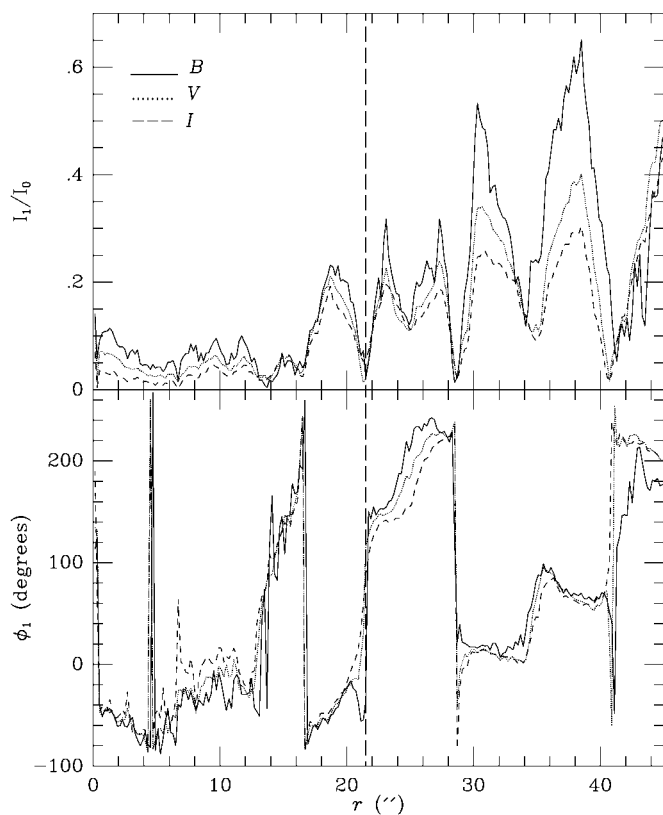


FIG. 11a

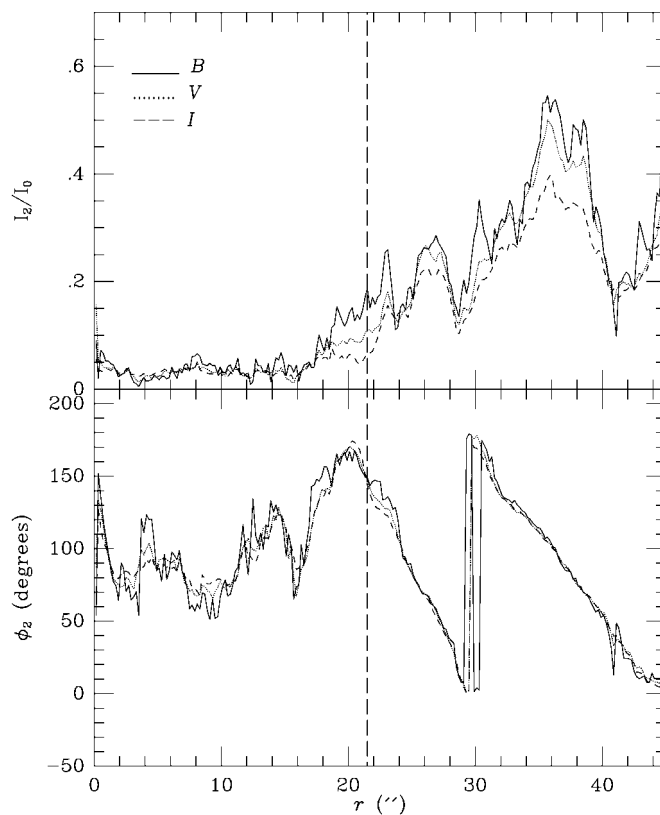


FIG. 11b

FIG. 11.—Relative Fourier amplitudes (intensity units) and phases for the (a) $m = 1$ component and (b) the $m = 2$ component. These are based on deprojected images assuming a major-axis position angle of 22° and an inclination of 19.3° . The phases are measured counterclockwise from the line of nodes, which was oriented vertically in the deprojected images. The vertical dashed line in each panel marks the boundary between the inner and outer spiral patterns.

the bulge is likely to be rounder than the disk, we have used the decompositions in Table 1 to subtract the bulge from the H -band light distribution, and then deprojected the residual disk light according to our orientation parameters. The disk potential in the plane of the galaxy was derived using the

method of Quillen, Frogel, & González (1994). The vertical density was assumed to be exponential with a scale height of 325 pc, similar to the scale height of the Galaxy (Gilmore & Reid 1983). The rotation curve of the disk was derived from the disk potential by computing a circularly averaged

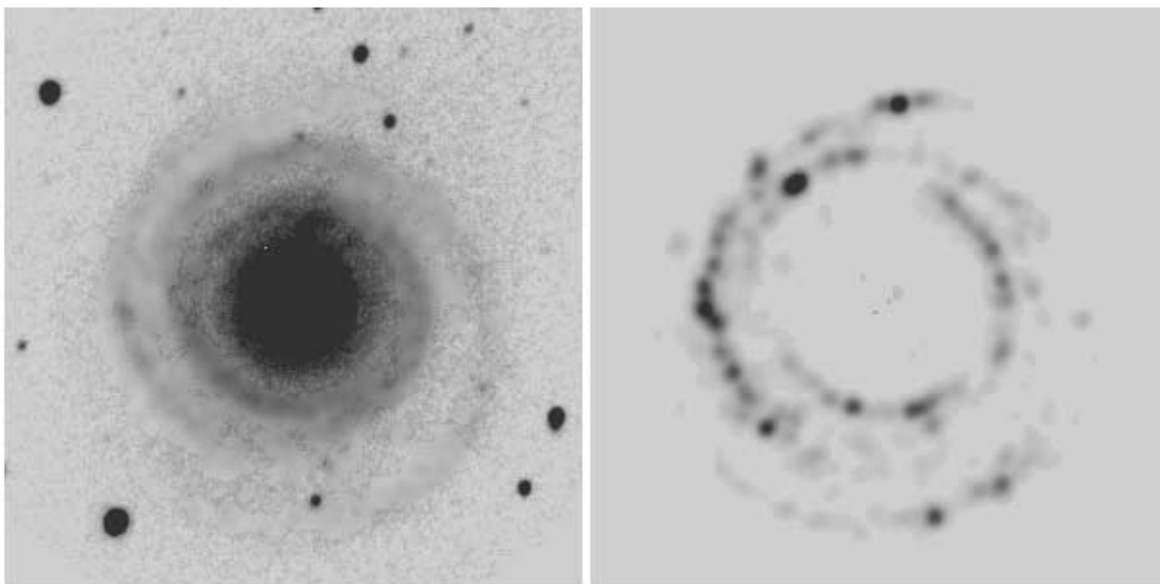


FIG. 12.—Left: Red continuum image of NGC 4622. Right: $H\alpha$ line-emission map of NGC 4622. Both are from Fabry-Perot interferometry. The field shown in each map is 1.96 square. North is to the top, and east to the left in these ground-based images.

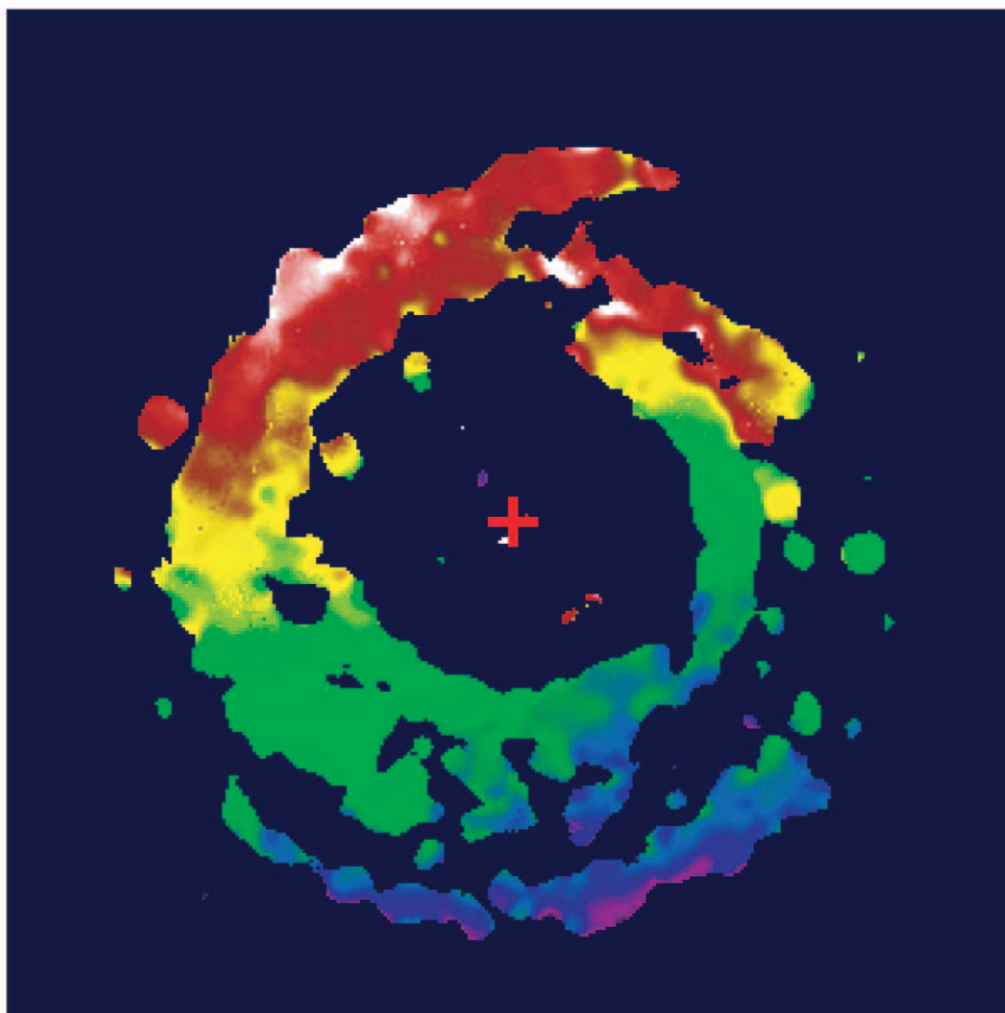


FIG. 13.—Radial velocity field of NGC 4622 from Fabry-Perot interferometry, color-coded so that reddish regions correspond to 4550 km s^{-1} and bluish regions to 4450 km s^{-1} . Orientation and field same as in Fig. 12.

potential profile as a function of radius. The rotation curve of the bulge was derived from the bulge decomposition parameters assuming the bulge is spherical, using a program from A. Kalnajs & S. M. Hughes (1984, private communication).

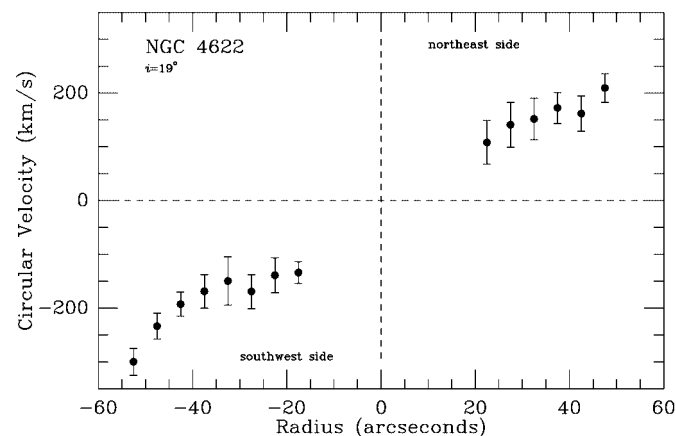


FIG. 14.—Rotation curve of NGC 4622 based on an inclination of 19° and a line of nodes position angle of 22° .

Figure 15a shows the combined rotation curve predicted from the H -band light distribution, assuming mass-to-light ratios $(M/L_H)_{\text{bulge}} = (M/L_H)_{\text{disk}} = 1.0$. This would be consistent with an old, single-burst stellar population having $[\text{Fe}/\text{H}] \approx 0$, based on the evolutionary synthesis models of Worthey (1994). The predicted combined rotation curve gives about the right $V_{c,\text{max}}$ if NGC 4622 is at the distance of $40.2 \pm 3.1 \text{ Mpc}$, but is inconsistent with the observed rotation curve. Whereas the predicted rotation curve is a normal, relatively flat one, with some decline in the outer

TABLE 2
FOLDED MEAN ROTATION CURVE OF NGC 4622 FOR $i = 19^\circ$

Radius (arcsec)	V_c (km s^{-1})	Number of Velocity Points	σ (km s^{-1})	Mean Error (km s^{-1})
17.5.....	131.4	117	24.6	2.55
22.5.....	131.6	2574	38.0	0.85
27.5.....	156.2	3895	39.3	0.69
32.5.....	152.0	4296	40.3	0.68
37.5.....	171.1	3994	29.5	0.51
42.5.....	183.6	2852	30.1	0.62
47.5.....	232.5	1462	24.4	0.70
52.5.....	299.8	78	24.9	2.94

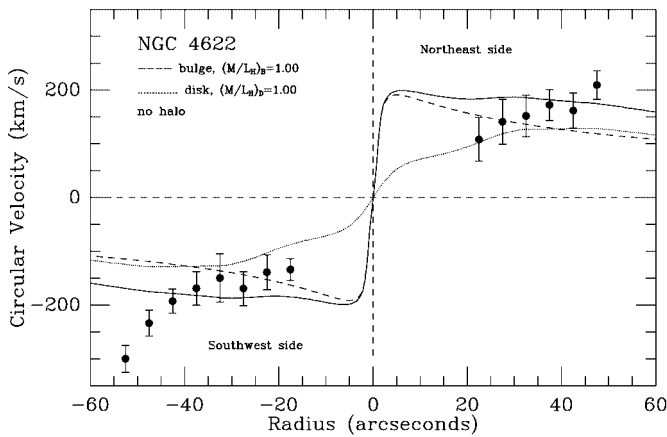


FIG. 15a

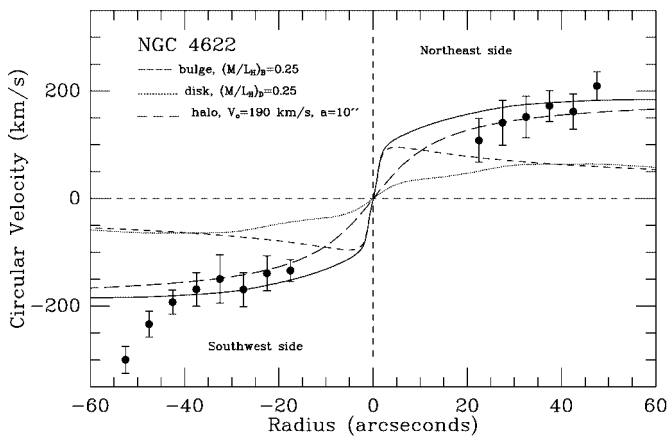


FIG. 15b

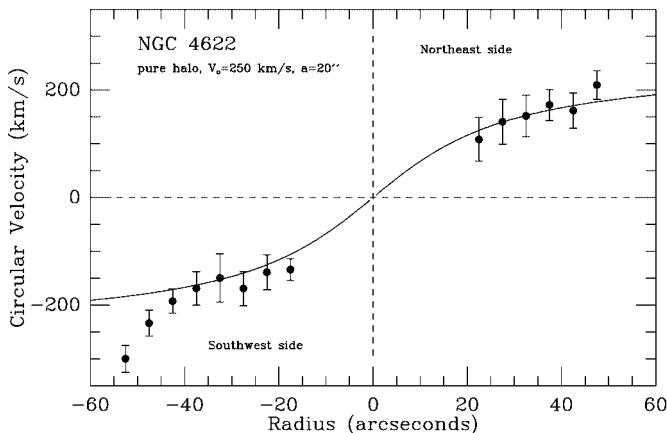


FIG. 15c

FIG. 15.—(a) Comparison between the rotation curve observed and the rotation curve inferred from the H -band light distribution, based on a mass-to-light ratio of 1.0 for both the bulge and the disk. (b) Comparison between the rotation curve observed and the rotation curve inferred from the H -band light distribution, based on a mass-to-light ratio of 0.25 for both the bulge and disk and a “fixed- σ ” halo component (Kent 1986) having the parameters indicated. (c) Comparison between the rotation curve observed and the rotation curve inferred from a pure “fixed- σ ” halo model having the parameters indicated.

parts likely due to the neglect of dark matter, the observed gaseous rotation curve is rising and does not intersect the predicted rotation curve until a radius of $35''$ – $45''$, on both sides of the major axis.

The only way to get the predicted rotation curve to approximate the observed one is to either reduce the mass-to-light ratio of the bulge or disk or both, or set this parameter equal to zero for both the bulge and the disk and consider a pure dark halo model. Since we have no rotation information inside the bulge-dominated area, we have little to constrain such a model. Nevertheless, Figure 15b shows a model where we have set the H -band mass-to-light ratio equal to 0.25 for both the bulge and disk and used a “fixed- σ ” model (Kent 1986) for the halo. The halo model shown has an asymptotic circular velocity $V_0 = 190 \text{ km s}^{-1}$ and a characteristic radius $a = 10''$. Although the model shows a general rise, it cannot reproduce the two points at $r > 45''$ on the southwest side. Figure 15c shows that a pure halo model could account for a rising rotation curve. However, the model shown has $V_0 = 250 \text{ km s}^{-1}$.

Among Sa spirals rising rotation curves are not infrequent, especially for the lower luminosity systems (Rubin et al. 1985). Kent (1988) shows that an extreme case, NGC 4698, has a rising rotation curve that is well-fitted by a constant mass-to-light ratio. Thus, the disagreement between the observed rising rotation curve and the one predicted from a constant mass-to-light ratio for NGC 4622 is probably significant.

5.3. The Impact of Streaming Motions in the Outer Arms

The rising rotation curve is an important finding from our study. It turns out that if the rise is real, we can much more easily explain the outer leading arms (Byrd, Freeman, & Buta 2003, hereafter Paper II). The implication would be that NGC 4622 has a very important dark matter contribution within the visible disk. However, the combination of noncircular motions and a low inclination could distort the observed rotation curve. There is some evidence for such motions in the northwest section of the disk where the observed velocities are higher than expected for pure circular rotation. We ask whether such motions (1) are explicable in terms of a density wave and (2) can explain the apparently rising rotation velocities.

First, it is important to note that streaming motions alone cannot resolve the issue of whether the outer arms are leading or trailing in NGC 4622. Consider a two-armed spiral that appears to open outward clockwise on the sky, as in NGC 4622. In the rotating reference frame of the spiral pattern, at least in linear theory, a two-armed trailing density wave rotating counterclockwise, confined entirely within corotation, and viewed with the west side as the near side would show the same pattern of streaming motions as a two-armed leading density wave rotating clockwise, confined entirely outside corotation and viewed with the east side as the near side.

The main question is whether we expect a substantial rise across the arms due to the perturbation. To examine this, we use the equations of linear density wave theory from Rogstad (1971), with a flat rotation curve set at 200 km s^{-1} , implied by the constant mass-to-light ratio analysis. Even with an assumed density contrast of 10 (the parameter c in Rogstad 1971), the main effect of the streaming motions is to cause “wiggles” across each spiral arm in the sense that, relative to the mean circular velocity, the residual velocities are positive on the inner edges of the arms and negative on the outer edges. The pattern seen in NGC 4622 is instead a general tendency for the velocities to rise across the arms.

Therefore, this rise is not likely to be an artifact of streaming motions.

6. THE SENSE OF WINDING OF THE SPIRAL ARMS OF NGC 4622

The information from surface photometry has shown that, while NGC 4622 has normal bulge/disk parameters for its Hubble type, its near-infrared photometric structure fails to account for its observed rotation curve. Even if we did not have any of this information, we could reliably deduce that NGC 4622 has leading spiral structure. As noted by Byrd et al. (1989) and by BCB, either NGC 4622 has a single inner leading arm and two normal trailing outer arms (scenario 1), or a single trailing inner arm and two very unusual bright leading outer arms (scenario 2). One of our goals in observing NGC 4622 with *HST* was to determine whether we could *prove directly* which of these two scenarios is correct. Although the first scenario is clearly more satisfying than the second, since it is theoretically much easier to make two strong trailing arms than two strong leading arms, we have chosen to be open-minded about the possibilities.

The ground-based Fabry-Perot velocity field has shown that gas clouds on the northeast side of the disk are receding from us relative to the systemic velocity. If we could determine which side of the disk is the near side, then we could determine directly which arms lead in NGC 4622. If scenario 1 is correct, then NGC 4622 would have to be rotating counterclockwise and the west side would be found to be the near side. If scenario 2 is correct, then the galaxy would have to be rotating clockwise and the east side would be found to be the near side.

The best way to determine the near side of a tilted disk is to look for a reddening and extinction asymmetry across the line of nodes. If the dust is confined to a thinner plane than the stellar disk and especially if a significant bulge is present, then the bulge is viewed through the dust on the near side and the dust is viewed through the bulge on the far side, leading to the reddening and extinction asymmetry. In early studies of this problem (e.g., Hubble 1943; de Vaucouleurs 1958) blue light images of highly inclined spiral galaxies showed the effect unambiguously, and it was concluded that all spiral arms are trailing. In no case was it ever suggested in these early studies that this method could be applied to a galaxy less inclined than 30° . In such galaxies it was not possible, with the old plates, to see the effect well enough for it to be unambiguous.

In NGC 4622 there are two factors that have a lot to do with our ability to see this effect. First, as we have shown, the bulge is a significant fraction of the total luminosity of NGC 4622. Second, the superior resolution of *HST* allows us to detect extremely weak dust lanes. We use two methods to investigate the dust and reddening in NGC 4622. The first is a $V-I$ color index map, shown in Figure 16. With the WFPC2 images obtained, this is the only color index map we can derive that has a high enough signal-to-noise ratio. The gray-scale in Figure 16 is coded such that red features are light and blue features are dark. The two solid white lines in Figure 16 show the position angle of the kinematic line of nodes, which in the frame of the WFPC2 images is tipped about 8° from vertical. The map shows obvious weak, thin dust lanes concentrated mainly on the east side of the line of nodes in the region of the inner ring

and between the nucleus and the ring. The west side also shows some dust lanes, but these appear much weaker by comparison.

In Figure 17 we show the V -band WFPC2 image of NGC 4622 after subtraction of the $m = 0$ Fourier component of the light distribution (*top right*, Fig. 9). In this map areas of extinction are clearly seen east of the line of nodes, with some strong regions of negative residuals close to the center. That these are generally also zones of reddening is verified by comparing Figures 16 and 17. Although the bulk of the apparent extinction and reddening is east of the line of nodes, we can still identify such regions on the west side of the line of nodes. For example, in Figure 16 dust patches can be seen to the northwest and southwest within $5''$ of the nucleus. However, the effects of these appear to be muted compared with the east side. Since the extinction and reddening asymmetries clearly appear to know the line of nodes, we conclude that the east side of NGC 4622 is the near side of its disk. With the ground-based velocity field, this would imply that NGC 4622 is rotating clockwise. *In this circumstance, our scenario 2 would be the correct one: the two strong outer arms would be leading, while the single inner arm would be trailing.*

Figure 18 shows a low-resolution $B-H$ color index map of NGC 4622. The line of nodes is indicated by the dashed black line. In spite of the low resolution, we can still detect a dust silhouette on the east side, to the left of the bright foreground star. However, if all we had was this map, we would not be able to use the reddening asymmetry method with confidence. High resolution was clearly needed to reveal the thin dust lanes on the near side.

A consequence of clockwise rotation of the disk is that not only are the two outer arms leading, but most of the thin arcs of dust on the east side would also be leading. Figure 16 shows one thin lane aligned perpendicular to the line of nodes, connecting a large dust patch near the line of nodes to a dust lane further out. This is an interesting peculiarity of the dust distribution, but most of the lanes simply arc like the spiral arms. Note that although the Galactic extinction toward NGC 4622 is significant ($A_V \approx 0.5$ mag), the scale of the thin lanes and their curvature like the arms rules out that they are Galactic in origin. This is verified also using Sky-View (McGlynn 2002)⁴ and *IRAS* 12–100 μm maps of the field around NGC 4622.

7. THE FEASIBILITY OF DETECTING A NEAR SIDE-FAR SIDE ASYMMETRY IN A LOW-INCLINATION GALAXY

It is reasonable to ask whether we should really expect to see a near side–far side asymmetry in a galaxy inclined as little as 20° . First we show that, with modern digital images, the effect can be very obvious in a galaxy inclined as little as 40° . The Ohio State University Bright Galaxy Survey (Eskridge et al. 2000) includes NGC 2775, one of the lowest-inclination galaxies considered by de Vaucouleurs (1958) for the dust silhouette method. Even in direct blue light plates NGC 2775 shows a clear arc-shaped dust silhouette on its west side (Sandage 1961). Based on his analysis of other galaxies, de Vaucouleurs suggested that the dust silhouette method might be applicable to NGC 2775 and that

⁴ Available at <http://skys.gsfc.nasa.gov>.

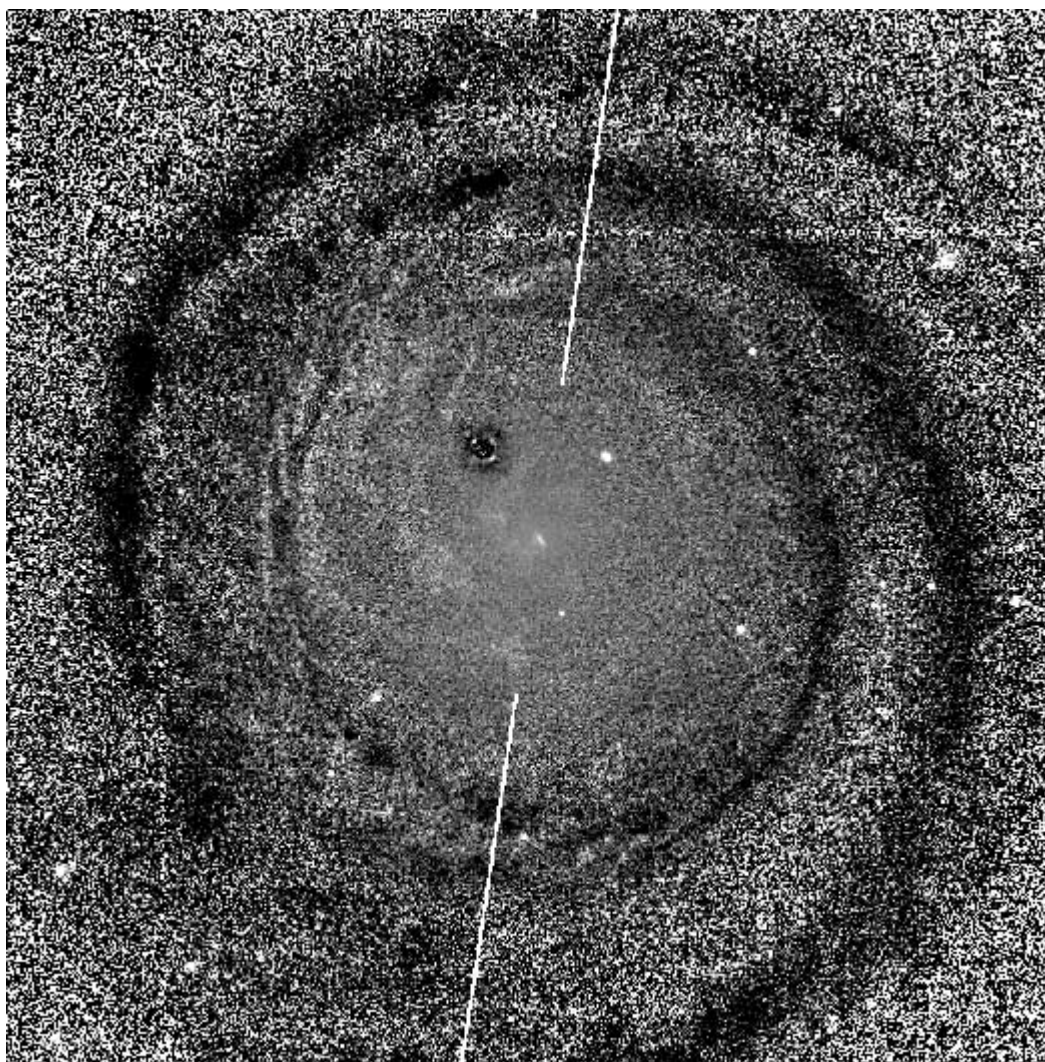


FIG. 16.—WFC2 $V-I$ color index map of NGC 4622. North is to the upper right, and east to the upper left, as in Fig. 1. The solid lines show the kinematic line of nodes for comparison, corresponding to an actual position angle of 22° . The map is coded such that redder regions are light and bluer regions are dark. It shows that thin dust lanes are confined mainly on the east side of the line of nodes. The field shown is 1.47 square.

the west side is its near side. However, he had no rotation curve for NGC 2775 to judge the sense of winding of its spiral arms. Figure 19 shows the OSU B -band image and a $B-H$ color index map of NGC 2775, the latter being coded such that red features are light and blue features are dark. The $B-H$ map shows a general reddening of the underlying light distribution on the west side and several dust arcs, including a complete dust ring that is enhanced on the west side. Based on this image, whose pixel resolution is only $1''.5$, the west side is obviously the near side. From ellipse fits to the B - and H -band isophotes on these images, we deduce that the inclination of NGC 2775 is only 40° . Like NGC 4622, NGC 2775 is a bulge-dominated galaxy, where the dust silhouette method can be applied in spite of a fairly low inclination.

Does this result for NGC 2775 imply nevertheless that we should see the effect if it were inclined only 20° ? At ground-based resolution we expect the effect would be difficult to detect, but the situation could be different at *HST* resolution. The best way to evaluate this is with an *HST*-resolution model that incorporates the known bulge and disk properties of NGC 4622 and that makes assumptions about the dust layer in the galaxy and the likely vertical

structure of the galaxy. The details of the model are described in Appendix A; here we only discuss the results. We examine the effect for four inclinations: 15° , 20° , 25° , and 30° . These should bracket the actual inclination of NGC 4622. Scattering is ignored in our analysis, but see Elmegreen & Block (1999) for models of near side-far side reddening asymmetries that account for single scattering, which can reduce the color asymmetry due to the general background dust layer by 10%–15%. The model includes a general dust layer and a series of four well-spaced, thin dust rings with widths comparable to those of the lanes seen on the east side in Figure 16.

Figure 20 shows model $V-I$ color index maps for the four inclinations, with a false color code chosen to enhance the near side-far side reddening asymmetry. The models are oriented so that the dust rings project into ellipses whose major axes coincide with the line of nodes of the galaxy. For each model, the near side corresponds to the left side (or east side on the sky). The maps show that we can detect a near side-far side reddening asymmetry, with the chosen optical depth parameters (see Appendix A), even for an inclination as low as 15° for *HST* resolution. The effect is weak at 15° but very obvious at 30° .

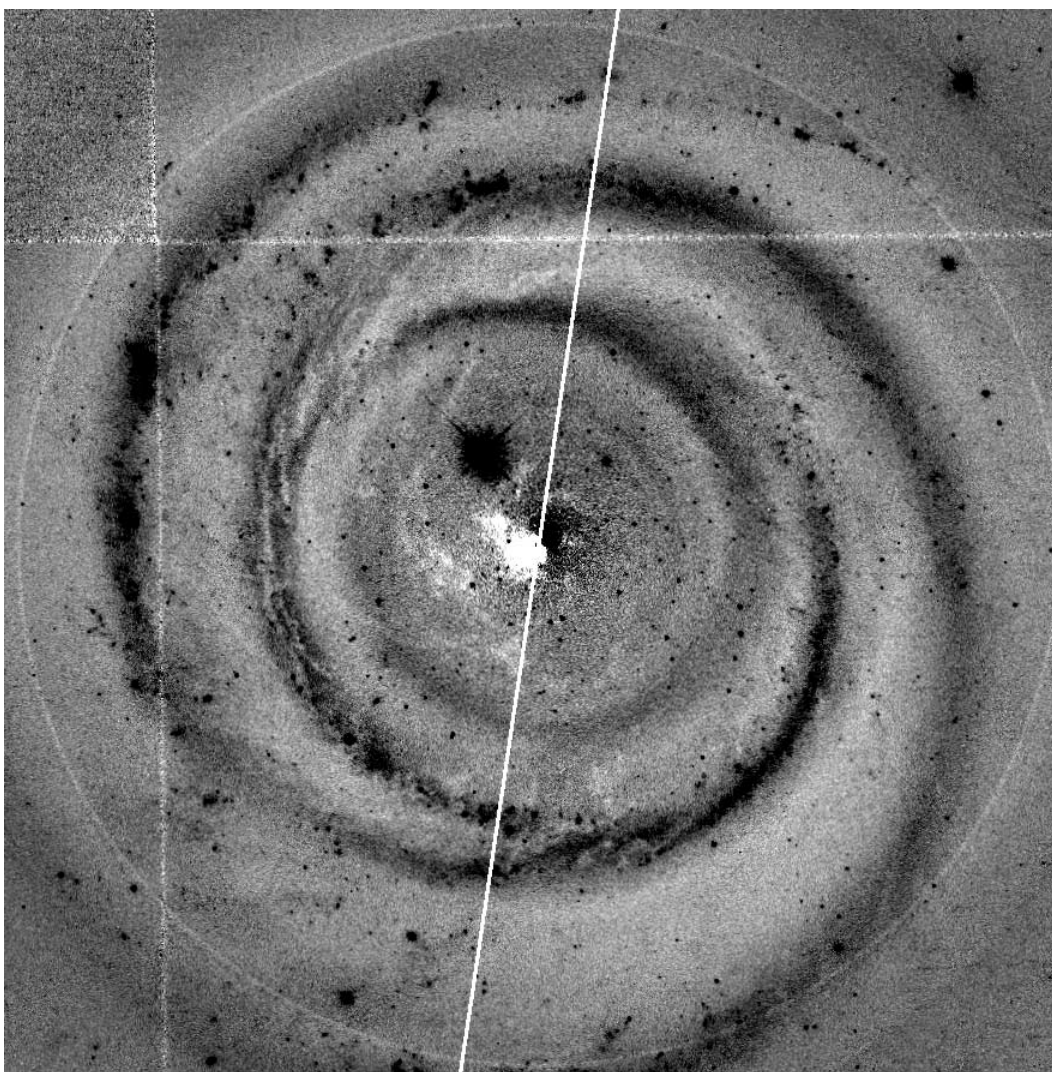


FIG. 17.—*V*-band WFPC2 map after subtraction of an $m = 0$ Fourier image. Orientation and field are the same as in Fig. 16. The solid white line is the kinematic line of nodes. The image shows again that the dust is mostly seen east of the line of nodes, but it also shows evidence for weaker dust lanes west of the line of nodes.

One way to compare these models with the actual galaxy is with surface brightness and color asymmetry curves. These do not supersede Figures 16 and 17 but serve to quantify the asymmetries along two axes. We assume initially that the galaxy is symmetric and that any residual asymmetry and reddening across the minor axis is due to our view through the dust layer. This assumption is valid at the 0.1 mag level only in the bulge-dominated region of NGC 4622, where isophotes are mostly centered on the nucleus. However, a nonuniform dust layer as well as intrinsic asymmetry can affect the asymmetry curves, and this plays a role at larger radii in NGC 4622.

Figures 21 and 22 show model surface brightness and color asymmetry plots across the kinematic minor axis for the four inclinations. The differences are

$$\Delta V = \mu_V(\text{east side}) - \mu_V(\text{west side}) ,$$

$$\Delta(V - I) = (\mu_V - \mu_I)(\text{east side}) - (\mu_V - \mu_I)(\text{west side}) .$$

The models were tilted so that the east side would be the near side. To improve the signal-to-noise ratio, we com-

puted average surface brightnesses along elliptical contours having major-axis position angle along the line of nodes, an axis ratio = $\cos i$, and within a cone having a half angle of 5° . The plots show the clear effects of both the dust rings and the general dust layer. The general dust layer causes ΔV and $\Delta(V - I)$ to be generally positive across the line of nodes. The amount of near side–far side extinction and reddening asymmetry increases with increasing inclination. The four dust rings show obvious excess extinction and reddening even at $i = 15^\circ$. Only the excess reddening due to the two outer dust lanes is lost in the noise at $i < 30^\circ$.

Figure 23a shows observed surface brightness and color asymmetry curves around the kinematic minor axis ($\phi = 112^\circ$) for NGC 4622. Again, to improve signal-to-noise ratio, we computed average surface brightnesses along elliptical contours having major-axis position angle along the line of nodes, an axis ratio = $\cos 20^\circ$, and within a cone having a half angle of 10° . It was necessary to remove the obvious globular clusters from the images before computing the asymmetry curves, since some of the clusters are bright enough to perturb the profiles.

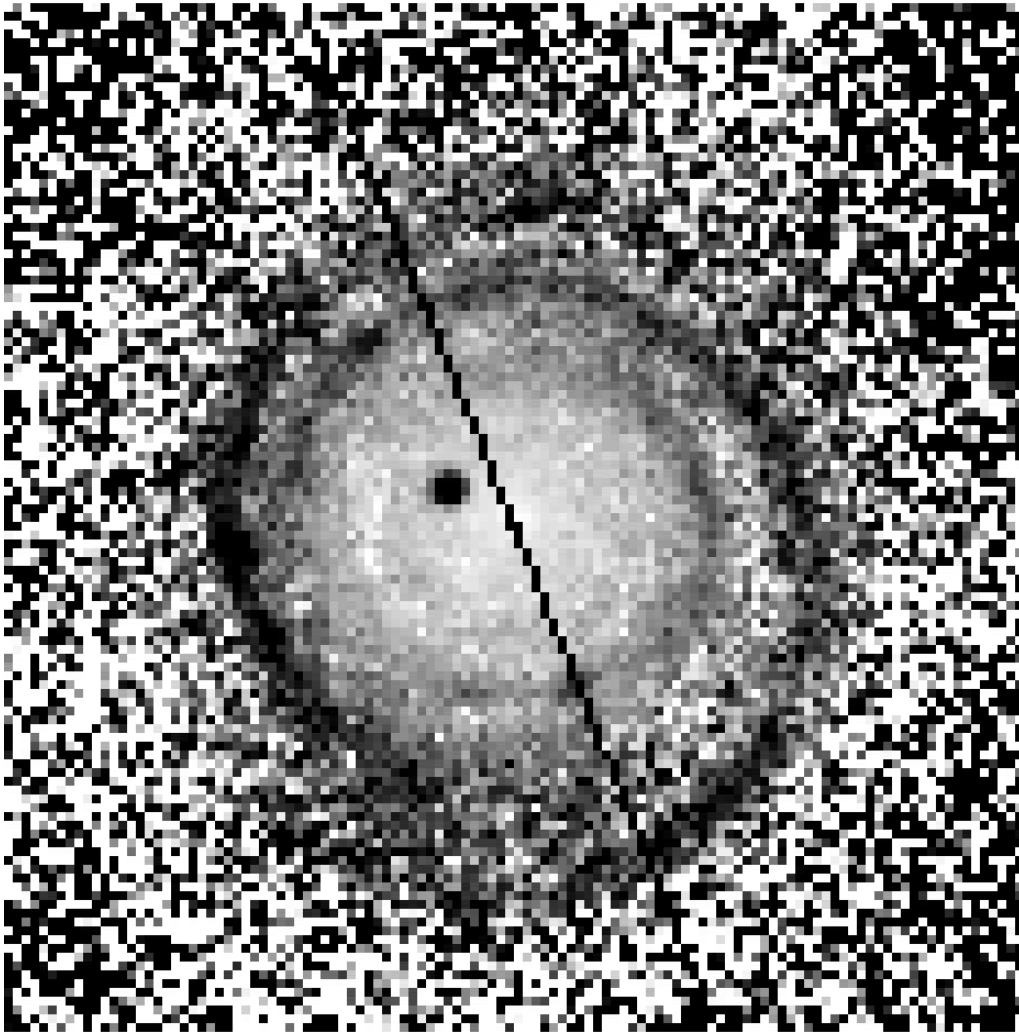


FIG. 18.—Low-resolution $B-H$ color index map of NGC 4622. The black ragged line shows the position angle of the kinematic line of nodes. The field shown is $2/43$ square. North is at the top, and east to the left in this ground-based image.

Figure 23a should be compared with the model asymmetry curves for $i = 20^\circ$ in Figures 21 and 22. In the bulge-dominated region, where the isophotes are reasonably well-centered on the optical nucleus, the extinction and color asymmetries are positive, as expected if they are due mainly to tilt and the east side is the near side. There is a slight excess of extinction and reddening between $8''$ and $12''$ radius. Beyond $12''$ there are more areas of reddening and extinction, but also areas of negative color and surface brightness differences. The negative ΔV values between $12''$ and $16''$ are due to the inner single arm. At radii approaching the optical ring and beyond the intrinsic asymmetries in the galaxy's spiral structure impact the asymmetry plots considerably, not just near side–far side effects. Nevertheless, even to a radius of $26''$ there is a general tendency for the galaxy to be redder on the east side.

These results support our conclusion that the east side of NGC 4622 is the near side. However, asymmetry curves taken along the kinematic *major axis* of NGC 4622 show surface brightness and reddening asymmetries similar to those seen along the minor axis. (No such differences are expected in our symmetric galaxy model.) Figure 23b shows the difference between the north and south halves of the

major axis. Within $r = 15''$, there is a slight tendency for the south half to be redder than the north half, although there is a more even distribution of positive and negative values of $\Delta(V-I)$ in the bulge-dominated region. The negative values of $\Delta(V-I)$ around $r = 9''$ along the major axis are due to a large obvious dust patch south of the center, seen in Figure 16. Although the effects we see are small, there does appear to be less average reddening from $r = 1''$ to $5''$ along the major axis compared with the minor axis. Thus, the complications along the major axis do not negate our conclusion that the east side is the near side. Again, we emphasize that these asymmetry curves do not supersede Figures 16 and 17, but merely quantify some of the differences seen.

8. THE GLOBULAR CLUSTER SYSTEM

We have noted that the spiral arms of NGC 4622 are lined by young associations, but in addition to these nearly starlike objects, the inner region of NGC 4622 is covered by a flurry of other faint starlike objects that are very likely to be globular clusters (see Fig. 10). This represents the first detection of a rich system of globular clusters in NGC 4622. In this section we wish to determine some of the properties of

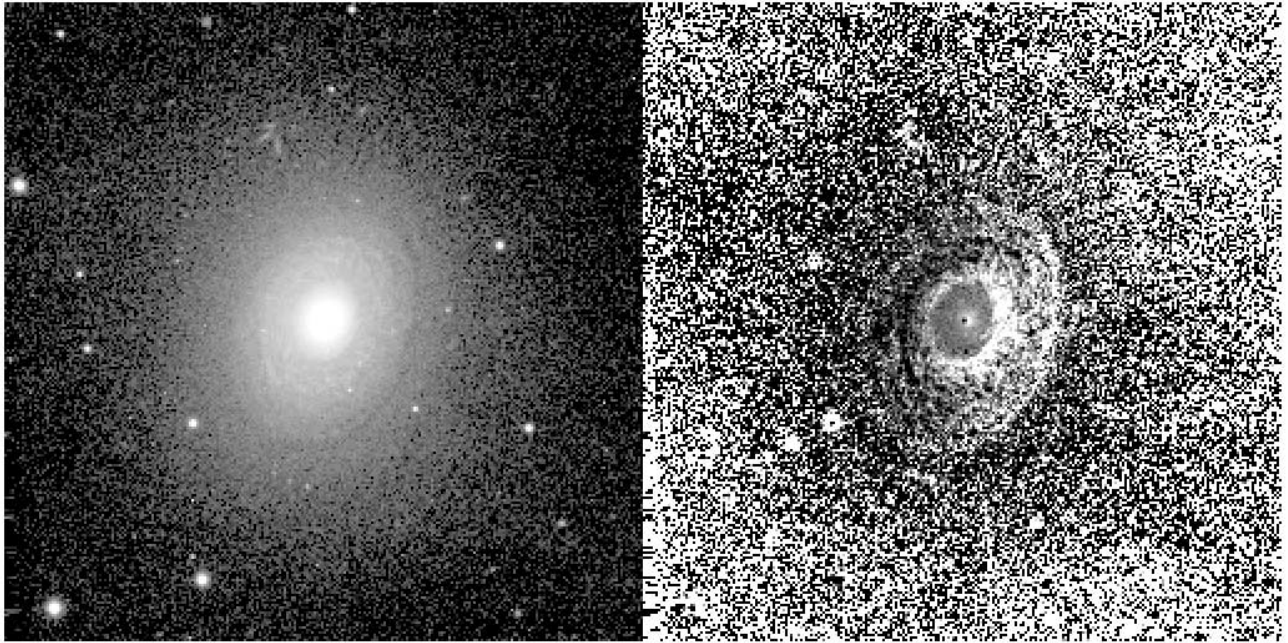


FIG. 19.—*Left:* B -band image of NGC 2775 from the OSU Bright Galaxy Survey. *Right:* $B-H$ color index map, coded such that redder regions are light and bluer regions are dark. Although the inclination is only 40° , this image conclusively shows that the west side of NGC 2775 is the near side. The field shown is 6.4 square. North is to the top, and east to the left.

this system, with the main goal being to verify the distance we are assuming for the galaxy. The associations are discussed in the next section.

The clusters were first isolated using the IRAF routine DAOFIND. In order to reliably detect the clusters superposed within the bright bulge area, the B , V , and I images were flattened by subtracting off the bulge and disk models of BCB. Since DAOFIND often misses some sources and finds some spurious sources, we corrected the output catalog by visual inspection of the images. The final catalog of sources included a mix of foreground stars, stellar associations, and globular clusters.

Photometry of the sources was performed with IRAF routine PHOT using an aperture radius of 2 pixels. This allowed us to use the formulae for charge transfer efficiency (CTE) corrections given by Whitmore, Heyer, & Casertano (1999). Aperture corrections to 0.5 radius were derived from foreground stars on the images since the clusters themselves are not resolved. For WF2–4, values of 0.19, 0.20, 0.20, and 0.24 mag were derived for filters F336W, F439W, F555W, and F814W, respectively. For the PC1, values of 0.42, 0.42, 0.42, and 0.58 mag were derived for the same filters. For Galactic extinction, we use the Schlegel et al. (1998) value of $E(B-V) = 0.139$ mag and use Tables 12a and 12b of Holtzman et al. (1995) to infer corrections to the natural WFPC2 systems. Since the Galactic reddening is fairly low, we averaged the implied extinctions in Tables 12a and 12b and used $AF_{336W} = 0.658$, $AF_{439W} = 0.578$, $AF_{555W} = 0.441$, and $AF_{814W} = 0.264$ mag. After an additional correction for decontamination, the corrected natural magnitudes were transformed to the standard systems using Table 7 and equation (8) of Holtzman et al. (1995).

Figure 24 shows a color-magnitude diagram for all sources having $V_0 \leq 25.0$. The absolute magnitude scale is

based on a distance of 40.2 Mpc. The diagram shows several well-defined regions:

1. A concentration of points having $V_0 > 21.5$ and $-0.5 < (V-I)_0 < 0.7$. These are mostly the young associations connected with the spiral arms and inner ring.
2. A concentration of points having $V_0 > 22.0$ and $0.7 < (V-I)_0 < 1.5$. These are the sources likely to be globular clusters.
3. Points of any magnitude having $(V-I)_0 > 1.5$ or points of any color having $V_0 < 21.0$ are likely to be foreground stars, background galaxies, or heavily reddened sources within the galaxy.

The likely globular clusters are isolated within the box in Figure 24. Figure 25 shows how the objects in the box are distributed within the WFPC2 field. To evaluate the contribution of field objects to the box, we show in Figure 26 the color-magnitude diagram of objects lying more than $65''$ (12.7 kpc) from the center. Even at these large radii the box shows a clear concentration of points that are not likely to be merely field objects. It appears the foreground star contamination in the box is low or insignificant. The galaxy clearly fills most of the WFPC2 field, and some likely clusters are found at large radii.

Figure 27 shows the distribution of $V-I$ colors for the 250 objects in the box. The solid curve is a Gaussian having $\langle (V-I)_0 \rangle = 1.04$ and dispersion $\sigma = 0.19$ mag. This is very typical of an old cluster system in an early-type galaxy (Kundu & Whitmore 2001). The mean color is consistent with a mean metallicity of $[Fe/H] = -0.98$ (Kundu & Whitmore 2001). However, there may be some dependence of the mean cluster color on radius. If we restrict the analysis only to the 27 clusters within the effective radius, $9.38''$ of the bulge, we get $\langle (V-I)_0 \rangle = 1.08$ and a dispersion of 0.14 mag. The slightly redder mean color could indicate that the

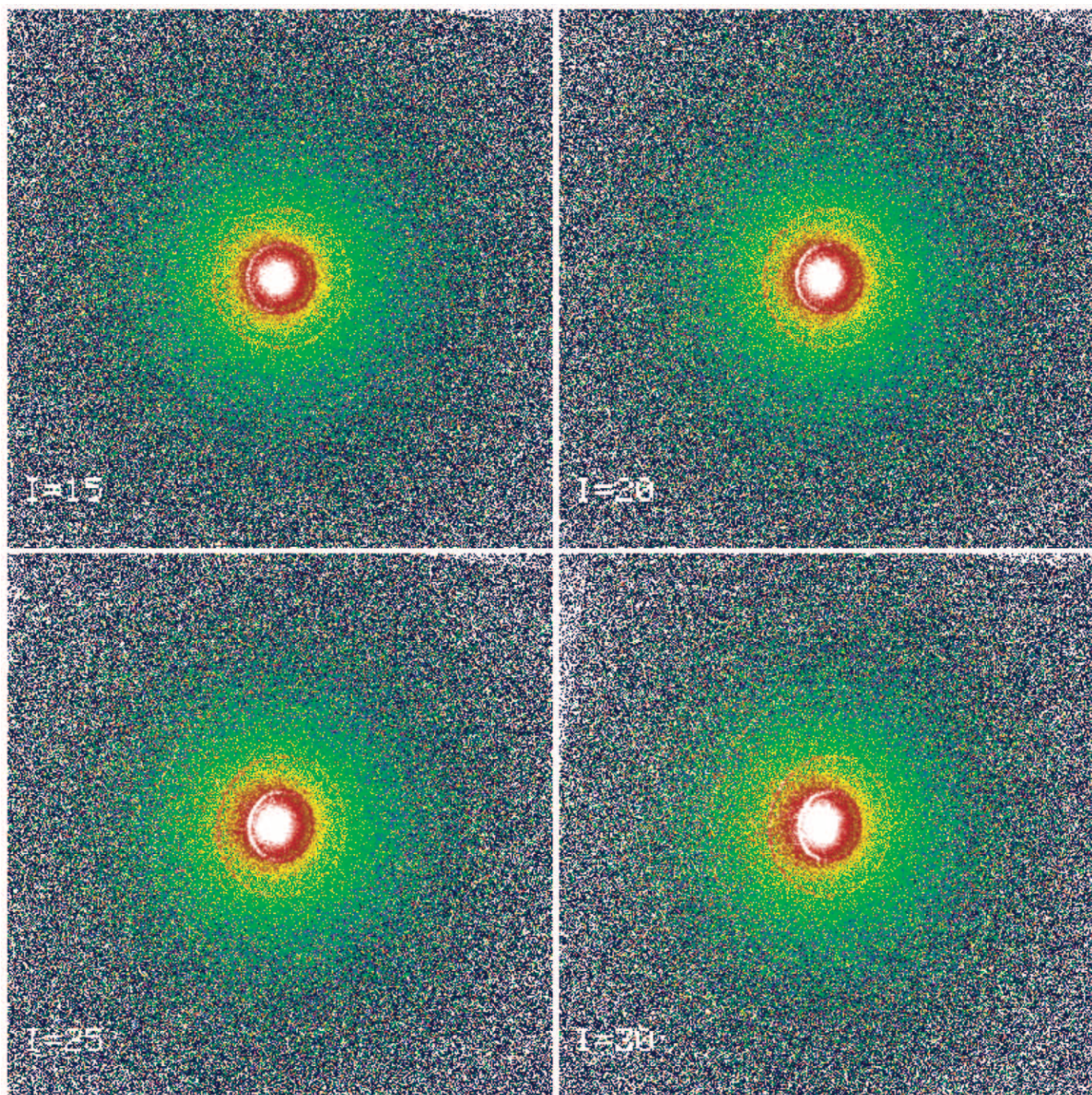


FIG. 20.—Model color index maps (excluding scattering) for four inclinations (upper left: 15° , upper right: 20° , lower left: 25° , lower right: 30°), with false color code to enhance the reddening asymmetry across the line of nodes (oriented at -7.5 in these images, the same as for the WFPC2 images of NGC 4622). Four dust rings were included in the model, the innermost one being most prominent in these maps. The noise level is approximately matched to that of the WFPC2 V -band image of NGC 4622. The assumed inclination is indicated in each panel.

metal-rich clusters in NGC 4622 are more centrally concentrated, as is often seen (for example, Larsen, Forbes, & Brodie 2001). However, bimodality is not obvious in Figure 27, although a more sophisticated statistical test (such as that described by Kundu & Whitmore 2001) might assess this possibility more objectively.

The luminosity function of globular clusters was derived by correcting the observed luminosity function for both areal incompleteness (due to the limited field of view of the WFPC2) and for detector incompleteness (due to the varia-

ble galaxy background). The detector incompleteness was evaluated using artificial cluster experiments. Since none of our photometric models fully accounts for the complex light distribution, we used the V -band WFPC2 image *cleaned of all stellar objects* for the test. The idea is that the cleaned V -band image provides the best background for any artificial cluster tests. The cleaning of the image involved a combination of PSF fitting and image editing. We created files with artificial clusters using a PSF based on several of the brighter clusters. We chose 12 intervals of 0.25 mag each

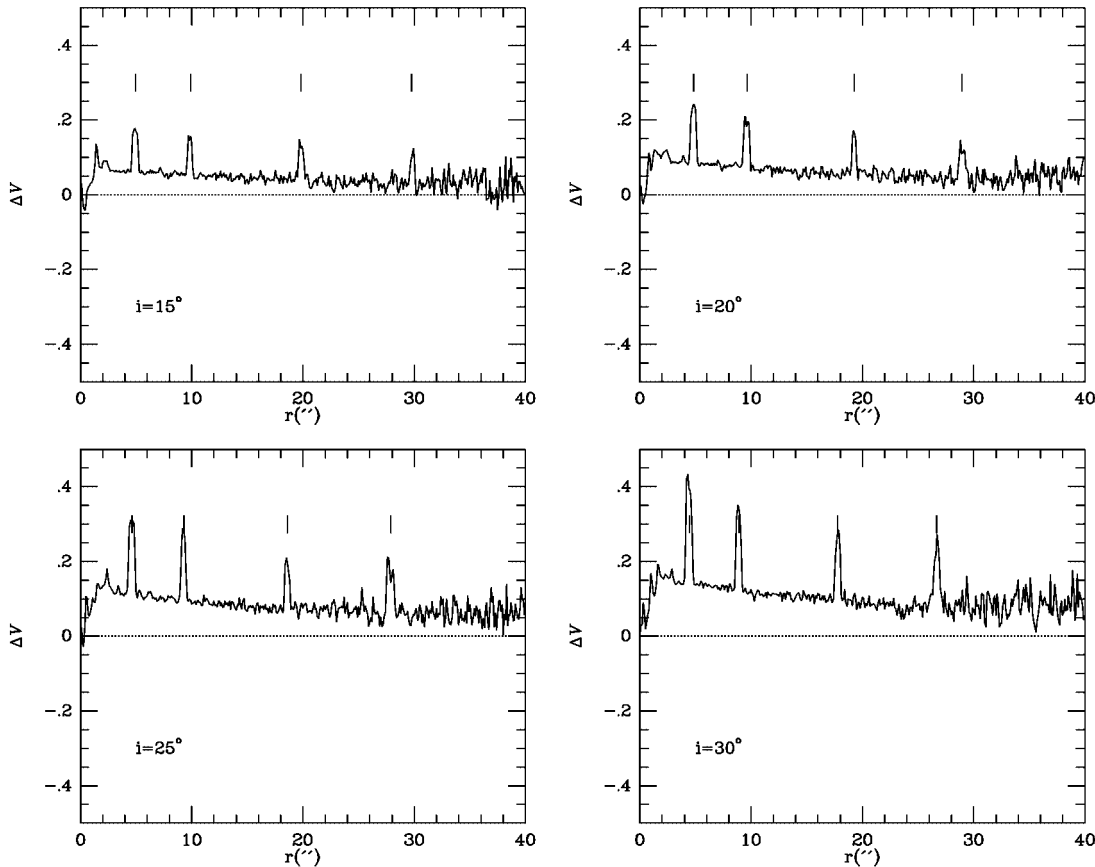


FIG. 21.—Plots of surface brightness asymmetry (in mag) along the minor axis (east side minus west side) for the four models in Fig. 20. The profiles are based on averages along contours having a major-axis position angle along the line of nodes and an axis ratio = $\cos i$, within a cone having a half angle of 5° . The short vertical lines refer to the positions of the model dust rings, which have a face-on optical depth τ_0 3 times that of the background dust layer.

from $V_0 = 22.0$ – 25.0 . Within each interval a random number generator was used to assign $V-I$ colors around a mean of 1.04 with a dispersion of 0.2 mag (the standard deviation about the mean color). Also, a random number generator was used to scatter artificial clusters across most of the WFPC2 field. For each magnitude interval, ≈ 3000 artificial clusters were used to judge completeness as a function of radius (which correlates approximately with background brightness) in intervals of $5''$ – $65''$ radius.

The artificial clusters were added to the cleaned V -band image using IRAF routine ADDSTAR. IRAF routine DAOFIND was used to locate the added clusters, whose coordinates were then matched with the input catalogue. Figure 28 shows the completeness curves for $V_0 = 23.00$ – 23.25 and 24.75 – 25.00 . The incompleteness is a function of both magnitude and background brightness, especially in the inner few arcseconds, where few clusters are found owing to the very high background brightness. To minimize the effect of photometric uncertainties, the analysis was restricted to $V_0 \leq 25.00$.

The areal correction affects only circular annuli whose radii exceed $43''$. Parts of these annuli are outside the WFPC2 field of view. The observed counts as a function of magnitude were then corrected for both this areal factor and the detector incompleteness functions for each magnitude interval. The corrected histogram of cluster magnitudes is illustrated in Figure 29, which shows that the turnover is not reached at the adopted magnitude limit. A Gaussian was fitted to the corrected distribution by fixing

the dispersion at $\sigma_{GC} = 1.3$ mag, characteristic of the globular cluster universal luminosity function (Kundu & Whitmore 2001). The turnover magnitude and the number count at this magnitude were then derived by nonlinear least squares. The turnover magnitude so derived is $\langle V_0 \rangle = 25.835 \pm 0.181$. If the intrinsic mean absolute magnitude is $M_V = -7.41$ (Kundu & Whitmore 2001), this implies a distance of 44.6 ± 3.7 Mpc, fully consistent with the Cen30 distance of 40.2 ± 3.1 Mpc that we have been assuming.

The specific frequency of clusters (number per unit $M_V = -15$ galaxy luminosity; Harris & van den Bergh 1981) was estimated by integrating the Gaussian fit in Figure 29, which implies the presence of 959 clusters (compared with the ≈ 250 brighter than $V_0 = 25.0$ within $r = 65''$). The total V -band magnitude estimated by BCB is $V_T = 12.41$. After correction for Galactic extinction, K -dimming, and inclination, the corrected V -band total magnitude is 11.88. Allowing for the uncertainty in $\langle V_0 \rangle$, the specific frequency is $S_N = 3.4 \pm 0.6$. This value is comparable, within uncertainties, to those for several large Virgo E's (Kissler-Patig et al. 1997) and to the Sombrero Galaxy M104 (Harris, Harris, & Harris 1984; Bridges & Hanes 1992). The referee suggests that this argues against any very recent major merger events or disruption. However, it does not necessarily rule out minor events involving small galaxies.

The completeness-corrected surface number density distribution of globular clusters is shown in Figures 30a and 30b. The surface density is plotted versus $r^{1/4}$ and versus

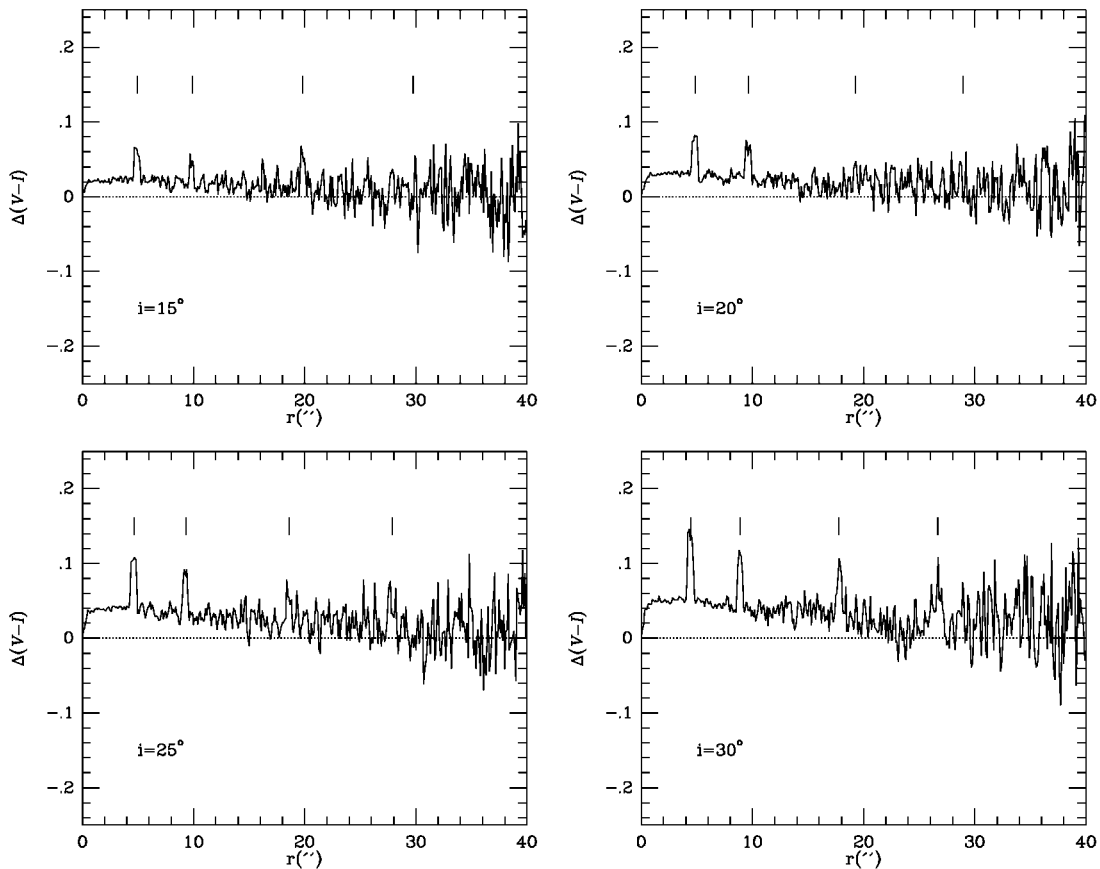


FIG. 22.—Plots of color asymmetry (in mag) along the minor axis (again east side minus west side) for the four models in Fig. 20. The profiles are based on averages along contours having a major-axis position angle along the line of nodes and an axis ratio = $\cos i$, within a cone having a half angle of 5° .

$\log R$, where R is in kiloparsecs based on a distance of 40.2 Mpc. Figure 30a shows that the surface densities approximately follow an $r^{1/4}$ law (*solid line*), but with a considerably larger effective radius than the underlying galaxy light distribution (*dotted line*). The solid curve in Figure 30b shows a King model fitted to the surface densities assuming a tidal radius $r_t = 50$ kpc. The core radius of the distribution is 3.1 kpc.

The larger effective radius for the globular clusters as opposed to the bulge light for NGC 4622 differs from the Sombbrero Galaxy, NGC 4594, whose globular cluster surface density distribution declines in a manner similar to the bulge light (Harris et al. 1984). Larsen et al. (2001) suggest that the clusters in that case are mainly associated with the bulge. The lack of agreement between effective radii for NGC 4622 suggests that the clusters are not simply associated with the bulge.

Finally, we ask whether the globular cluster system supports our interpretation of the east side being the near side of the galaxy. If the clusters are distributed more spherically than the disk, we should see a near side–far side extinction and reddening asymmetry similar to what we see in the light distribution. Figure 31 shows histograms of the number of clusters as a function of radius, with the solid histogram including only clusters east of the kinematic line of nodes and the dashed histogram including only clusters west of the line of nodes. The plot shows that the east side has more clusters in the $0''$ – $5''$ bin (see also Fig. 10), while, farther out, there tends to be more clusters west of the line of nodes. In

the $10''$ – $15''$ bin, there are few clusters in the obvious dust lanes on the east side. For 46 east side clusters within a radius $r = 20''$, the mean $V-I$ color index is 1.077 ± 0.022 , while, for 47 clusters west of the line of nodes within the same radius, the mean $V-I$ color is 1.057 ± 0.022 . Thus, only a small and insignificant reddening difference is found between near-side and far-side clusters.

In summary, we find a rich globular cluster system in NGC 4622 with fairly normal properties. We do not detect obvious bimodality in its color distribution, which would imply that no new globular clusters have formed in the last few billion years.

9. STAR FORMATION IN NGC 4622

Most of the objects in the region $21.5 \leq V_0 \leq 25.0$, $-0.5 \leq (V-I)_0 \leq 0.7$ in Figure 24 are likely to be young stellar associations. This is verified in the two-color plots in Figure 32. The errors increase rapidly with increasing magnitude; thus, Figure 32 shows the plots for two different intervals: $21.5 \leq V_0 \leq 23.0$ and $23.0 \leq V_0 \leq 24.0$. Some of the excess scatter in these plots is due to the limitations of using aperture photometry for the measurements of such associations, which may have multiple components. Based on comparisons with the solar metallicity, Salpeter IMF models of Bruzual & Charlot (1996; *solid curves*, Fig. 32), most of the brighter associations are probably less than 10 Myr old. The two reddest objects in the left panels of Figure 32 could be affected by a higher than average reddening

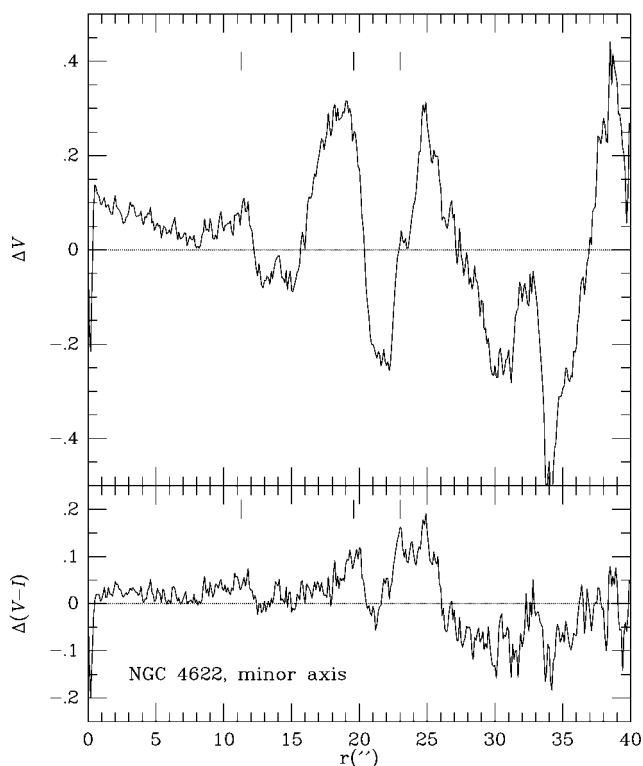


FIG. 23a

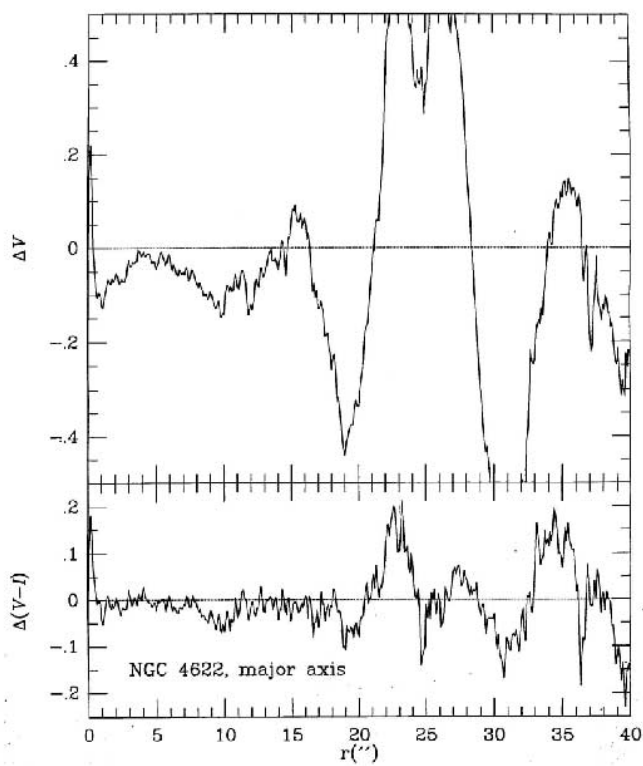


FIG. 23b

FIG. 23.—Plots of WFPC2 surface brightness and color asymmetry along the kinematic minor (*a*) and major (*b*) axes of NGC 4622. The profiles are based on averages along contours having a major-axis position angle along the line of nodes and an axis ratio = $\cos 20^\circ$, within a cone having a half angle of 10° . The short vertical lines in (*a*) point to dust features seen in the images. The differences are in the sense east minus west for the minor axis, and north minus south for the major axis.

compared with most of the other points (see reddening lines in the right panels, for example). The characteristics of the star formation in NGC 4622 can be summarized as follows:

1. The WFPC2 *U*-band and ground-based $H\alpha$ (Fig. 12) images reveal considerable asymmetry in the distribution of

young associations. These associations are numerous along the east outer arm and along the northern section of the west outer arm.

2. There is a very thin ridge of star formation along the concave edge of the north section of the east outer arm (see

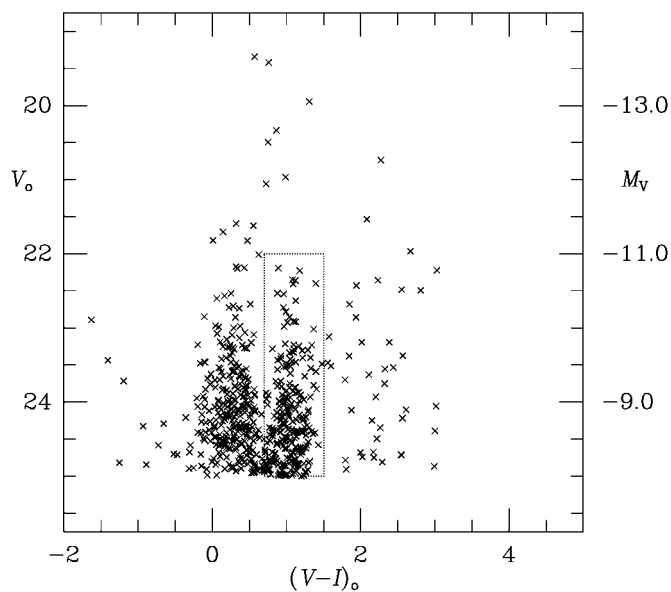


FIG. 24.—Color-magnitude diagram of point or near-point sources in the WFPC2 field of NGC 4622. The dotted box isolates the objects that are likely to be globular clusters. The absolute magnitude scale is based on a distance of 40.2 Mpc.

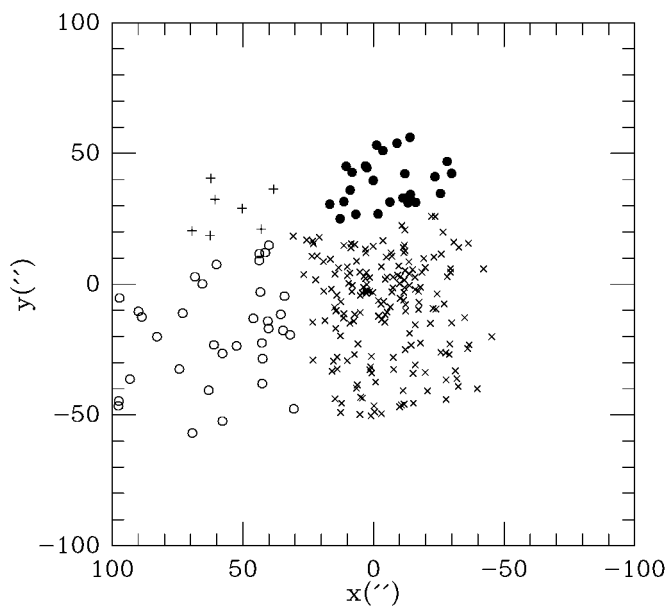


FIG. 25.—Distribution of the 250 objects lying within the dotted box in Fig. 24. Crosses refer to WF3, filled circles to WF4, open circles to WF2, and plus symbols to PC1. Coordinates are relative to the nucleus, and the plot has the same orientation as the image in Fig. 1.

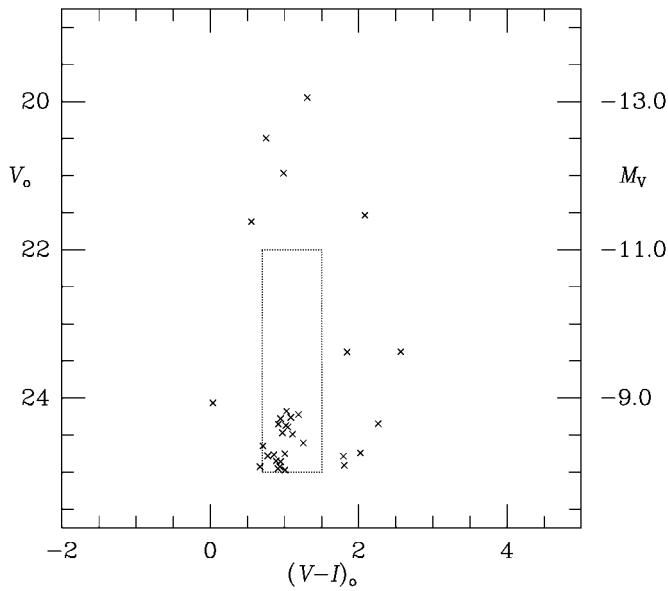


FIG. 26.—Color-magnitude diagram of sources having $r > 65''$ within the WFC2 field. The dotted box is the same as shown in Fig. 24 and probably includes mostly globular clusters.

Fig. 33, feature labeled “1”), extending from near the line of nodes (nearly vertical) to about due north of the nucleus. This ridge looks almost detached from the stellar background part of the arm in this region.

3. Moving further counterclockwise along this arm, the associations are less offset from the concave edge, so that, by the south part of that arm, some of the associations are actually on the convex side (Fig. 1).

4. Beginning at about the line of nodes and going counterclockwise, the star formation in the west outer arm lies near the convex edge of the arm, completely the opposite of

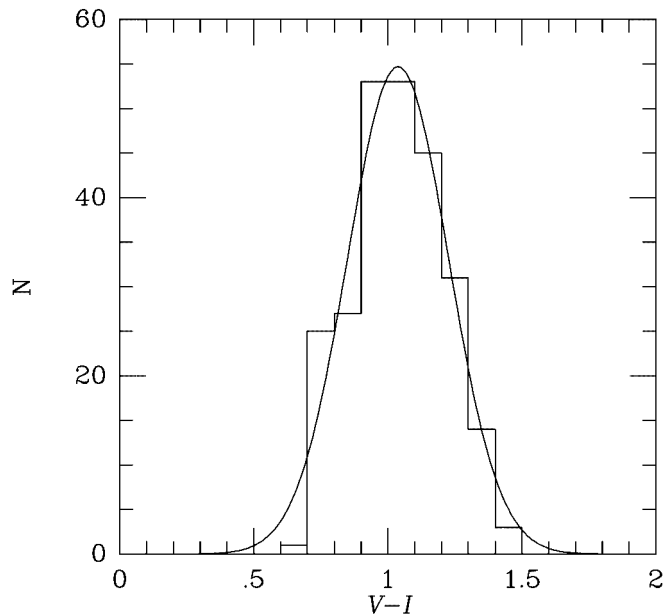


FIG. 27.—Distribution of $(V-I)_0$ colors of the objects within the dotted box in Fig. 24. The solid curve is a Gaussian fitted to the histogram. The mean, 1.04, and dispersion, 0.19, are typical of old globular cluster systems seen in other galaxies (Kundu & Whitmore 2001).

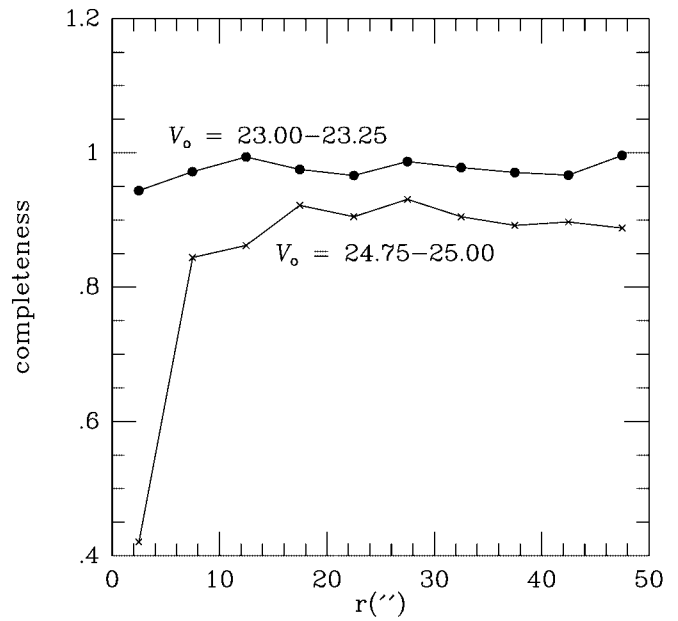


FIG. 28.—Completeness curves for two magnitude intervals to show how the detectability of the globular clusters depends on both magnitude and background brightness.

the east outer arm in the same general area (see Fig. 33, feature labeled “2”). Further clockwise along this arm, associations are few and tend to lie either within the arm or near its concave edge (Fig. 1).

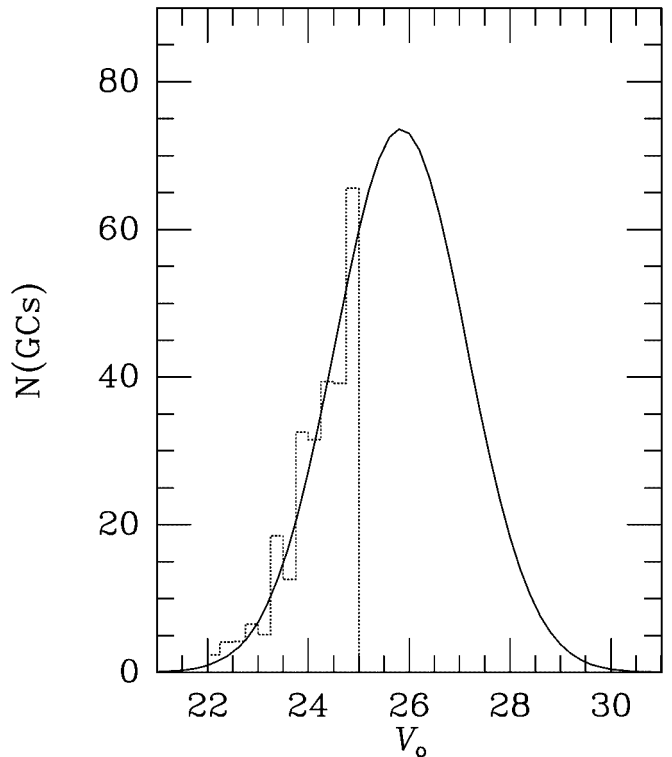


FIG. 29.— V -band luminosity function of globular clusters in NGC 4622, corrected for both areal and detector incompleteness. The solid curve is a Gaussian fit to the histogram having a fixed dispersion of $\sigma = 1.3$ mag.

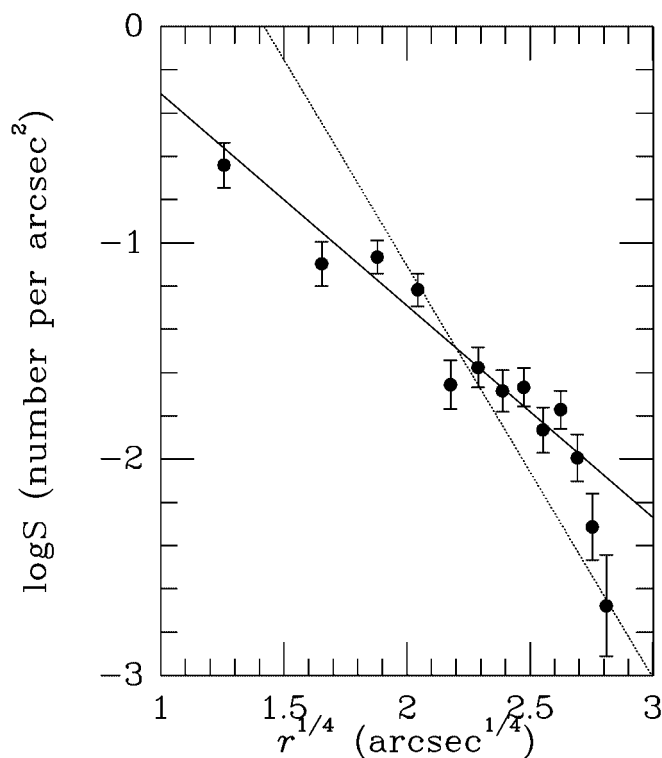


FIG. 30a

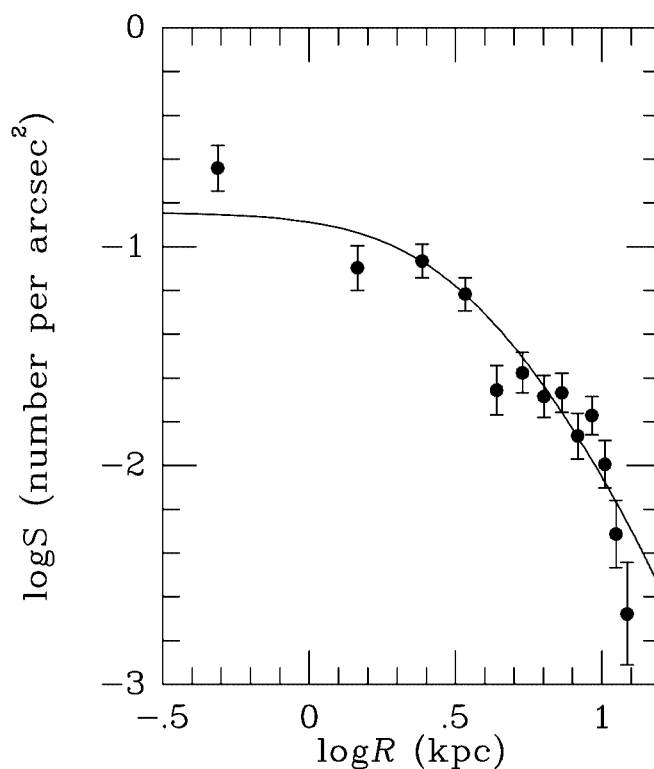


FIG. 30b

FIG. 30.—(a) Surface density of globular clusters in NGC 4622 versus $r^{1/4}$ in projection, where r is the radius in arcseconds. The solid line is a weighted fit to an $r^{1/4}$ law to the observed points. The dotted line shows the fit forced to have the same slope as the background starlight. (b) Same as (a) but the curve now represents a fit of a King model to the surface densities. In this case the radius R is in kiloparsecs.

5. The star formation within the inner ring is complex. There are virtually no blue associations along the northeast half of the ring (region 3 in Fig. 33). This is also the half that is riddled with dust lanes on the proposed near side.

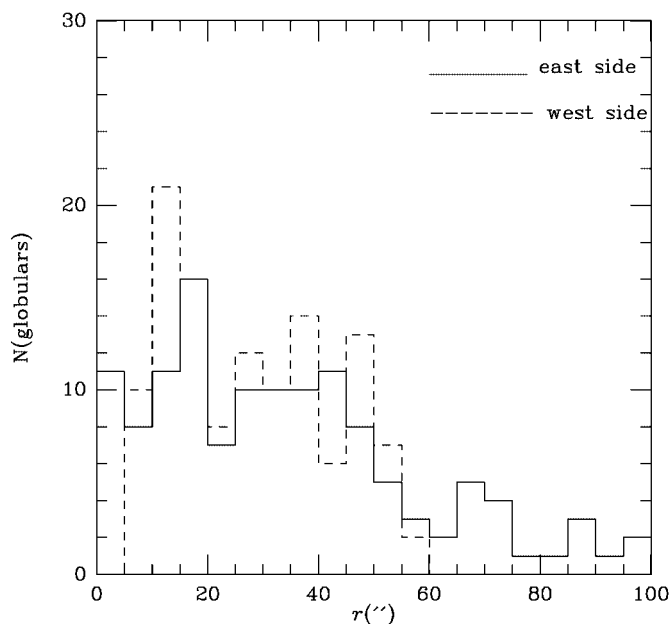


FIG. 31.—Histograms of the numbers of globular clusters east (solid line) and west (dotted line) of the kinematic line of nodes.

The reddening on the east side of the inner ring thus can partly explain the one-fold variation in color around the ring found by BCB (their Fig. 11d). However, the asymmetry is not entirely due to dust, because the part of the ring due north of the nucleus shows little evidence for dust and no bright young associations (region 4 of Fig. 33). Figure 34 shows color index versus position angle around the ring, based on the WFPC2 data. These curves were derived by first making a visual mapping of the ring on the V -band WFPC2 image, fitting an ellipse to its shape, and then circularizing the ring using IRAF routine IMLINTRAN. The ellipse fit gave a center displaced by $\Delta x = 1''.33$ and $\Delta y = -2''.14$ (in WFPC2 frame), and an axis ratio of 0.91. On the circularized ring, a series of circular apertures $3''.0$ in diameter was placed around the ring in 1° steps. Figure 34 shows the approximately sinusoidal variation in color that distinguishes the inner ring from features seen in other galaxies (Buta & Combes 1996; Buta & Purcell 1998). The youngest (bluest) associations that appear to be part of the inner single arm are on a southern portion of the inner ring. These coincide with bright H II regions in Figure 12.

10. DISCUSSION

10.1. The Viability of Strong Leading Arms in NGC 4622

The possibility that two very strong, obvious outer spiral arms in a fairly normal looking galaxy are leading is clearly unprecedented and questionable even on fairly simple grounds. In their discussion of density wave theory Binney & Tremaine (1987) argue that leading arms are not likely to be seen because they would quickly unwind and become

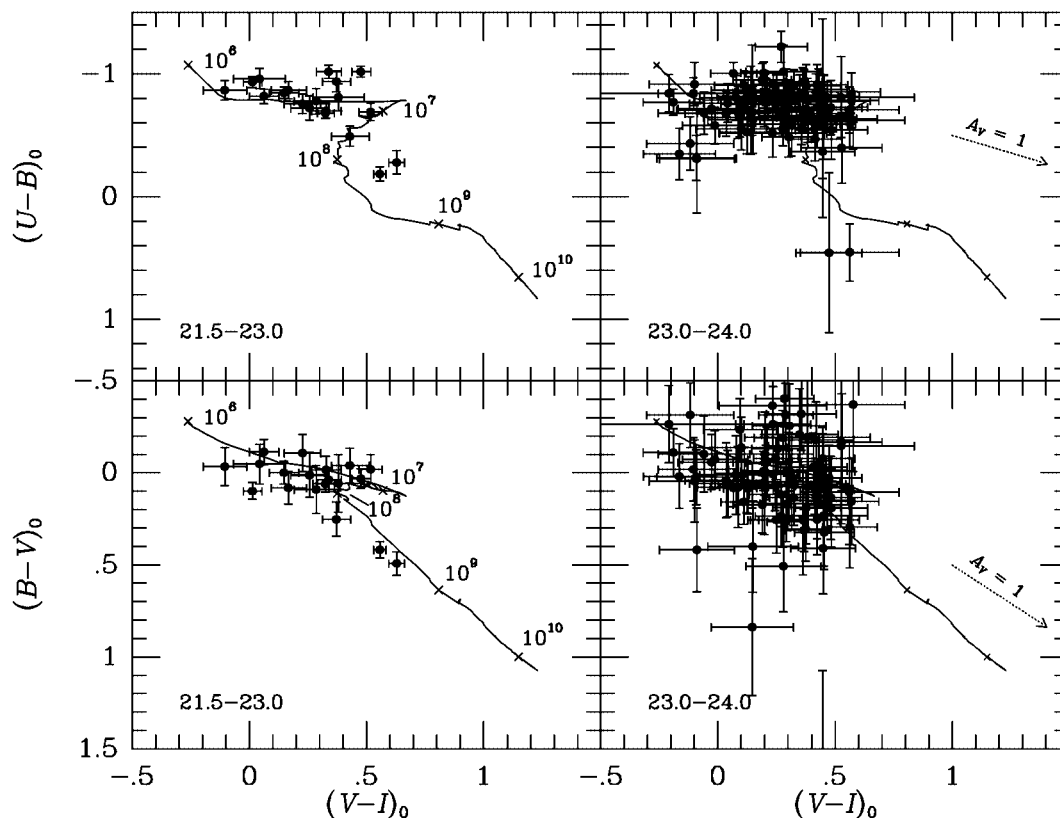


FIG. 32.—Two-color plots of those sources in Fig. 24 having $21.5 \leq V_0 \leq 23.0$ (left) and $23.0 < V_0 \leq 24.0$ (right) in the color range $-1 \leq (V-I)_0 \leq 0.7$. The solid curves in each plot are evolutionary synthesis models (for solar metallicity and a Salpeter IMF) from Bruzual & Charlot (1996; see also Buta et al. 2001). Several points on the curves in the left panels are labeled by the cluster age in years. Reddening lines are shown for a visual extinction $A_V = 1$ mag in the right panels. These plots confirm that most of the sources in the region to the left of the dotted box in Fig. 24 are young stellar associations.

trailing arms. Indeed, the swing amplifier mechanism of Toomre (1981) depends on this change, which is accompanied by a significant amplification of the resulting trailing arms.

The method we have used to deduce the sense of rotation of the disk of NGC 4622 is the same one that was used for the generally accepted conclusion, noted by Binney & Tremaine, that all spiral arms trail. This conclusion is largely

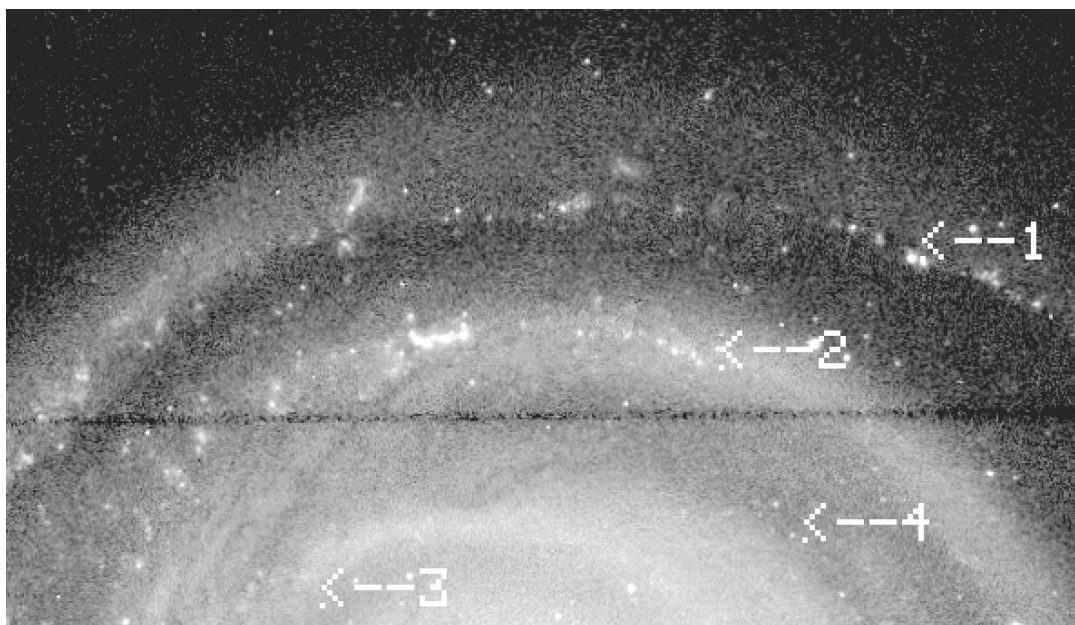


FIG. 33.—Close-up of northeast part of NGC 4622 (F555W filter) showing star-forming ridges. Features labeled 1–4 are discussed in the text. The area shown has dimensions 0.99×0.57 . North is to the upper right, and east to the upper left, as in Fig. 1.

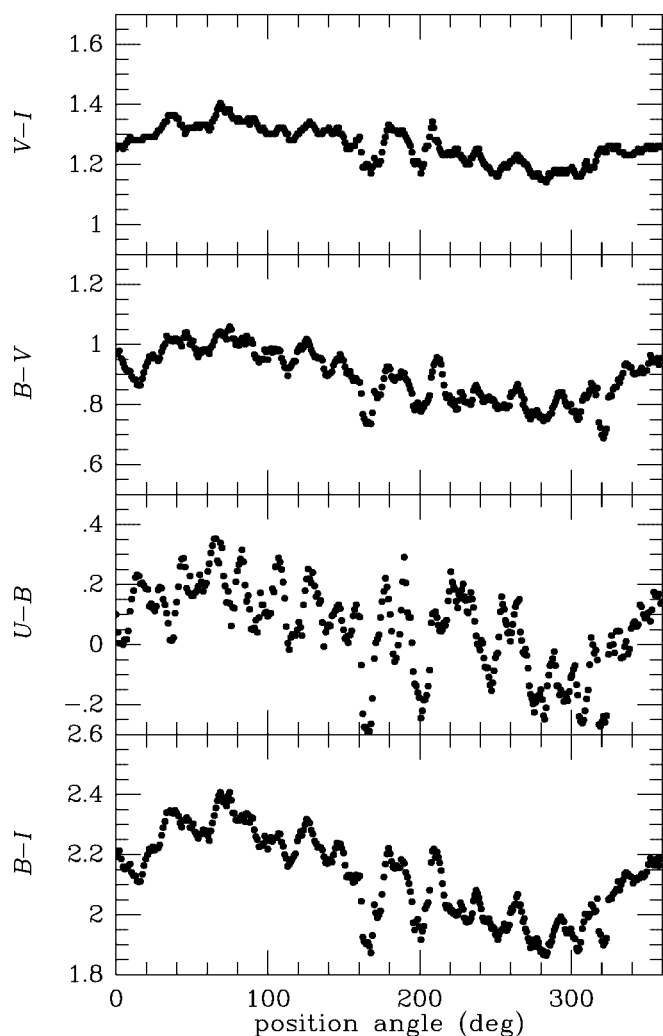


FIG. 34.—Color index vs. position angle around the inner ring of NGC 4622, based on WFPC2 images. The position angle is measured relative to true north.

based on the papers of Hubble (1943) and de Vaucouleurs (1958), who used samples of one to two dozen galaxies having rotation data and high quality photographic plates. The assumptions in determining the near side from an absorption asymmetry are that the dust layer is confined to a thinner plane than the disk and that the bulge is a more three-dimensional component than is the disk. The galaxies de Vaucouleurs and Hubble used were highly inclined, and most were not exceptional examples of spiral galaxies. (In fact, three of de Vaucouleurs's galaxies are now recognized as flocculent spirals.) Although high inclination makes it difficult to see the spiral arms of a galaxy, we have shown that low inclination does not preclude using the near-side absorption technique when the bulge is especially significant and the image resolution is high. Thus, we believe there is no ambiguity in the case of NGC 4622. The data favor the east side as the near side, and the outer arms are leading.

An important question to ask is whether any other aspect of the spiral structure of NGC 4622 supports this conclusion. For example, for trailing density waves lying inside corotation, a star or gas cloud first encounters the wave on its concave side. A shock would lead to an asymmetric azimuthal profile across the arm beginning with a sharp peak

followed by a gradual decline in the direction of rotation (Schweizer 1976). The presence of sharp dust lanes on the concave sides of spiral arms is often taken to be the shocks expected, with the young stars appearing further into the arms. Galaxies such as M51, M101, and M83 show this effect fairly well (Sandage 1961).

In NGC 4622 the east outer arm shows a strong ridge of star formation on its concave northern edge that is qualitatively similar to this kind of expectation (feature labeled “1” in Fig. 33). What appears to be lacking is a clear concave dust lane; in fact neither of the two outer arms shows such lanes, which tend to be more evident in late-type spirals. If the east outer arm lies within corotation, then one could argue that it would have to be trailing in order for the star formation ridge to be located on its concave edge. In contrast, the main star formation connected with the west outer arm (feature labeled “2” in Fig. 33) lies on its outer edge. If it is a trailing arm, then it would have to lie outside corotation to show such an effect. Since this is contradictory (the outermost portion of the east arm cannot be inside corotation while the innermost portion of the west arm, at a smaller radius, is outside), we would have to conclude that the arms are not trailing. The contradiction would be removed if the two outer arms are leading density waves, because then corotation could be between features 1 and 2 in Figure 33. This is discussed further in § 10.4.

Toomre (2002, private communication) argues that the character of the dust lanes in the east section of the inner ring favors that the galaxy is rotating counterclockwise. These dust lanes include short spurs that are tipped in the same sense as the outer spiral arms, i.e., open outward in a clockwise direction, and, as we have already noted, the color index map also shows that most of the small dust features, with one likely exception, would be leading if the galaxy is rotating clockwise. According to Toomre, the short spurs “look awfully much like other relatively small-scale results of swing amplification of gas plus dust inhomogeneities due not only to their own self-gravity but also some of the passing stars in this galactic shear flow, much like the spiral wakes of Julian & Toomre (1966), and any such rudimentary features simply have to be trailing themselves, regardless of any minor merging or interplay that probably did confuse this galaxy as a whole.” However, this interpretation, as straightforward and logical as it may seem, leaves two issues unexplained: why does the apparent dust distribution know the line of nodes, and why is the inner arm allowed to open in the opposite sense?

The single inner arm is not likely to be a leading component caught before it swings and amplifies. Indeed, in the swing amplifier theory of Toomre (1981), it is a two-armed leading spiral that swings into a much stronger two-armed trailing spiral, the result of a conspiracy between shear, epicyclic motions, and self-gravity of the arms. In NGC 4622 the maximum relative amplitudes of the $m = 1$ inner spiral and the $m = 2$ outer spiral differ only by a factor of about 2 in I (see Fig. 11, by comparing the $m = 1$ maximum at $r = 19''$ with the $m = 2$ maximum at $r = 36''$). One could therefore ask whether it is theoretically more reasonable that the inner single arm has the leading sense. The feature is weaker and has little gas, except where it overlaps the inner part of the west outer arm; it therefore might be less troublesome to be leading than the two strong outer spiral arms. There is no question of the reality of the inner arm as a genuine spiral feature in NGC 4622. Although single-

armed leading spirals have been shown to result from retrograde tidal encounters (e.g., Athanassoula 1978; Byrd et al. 1993; BCB and other references therein), it does not follow that all observed single arms must be leading (e.g., Byrd, Freeman, & Howard 1994). For example, the dust silhouette technique combined with a published $H\alpha$ rotation curve indicates that the single spiral arm seen in NGC 4378 is trailing (Byrd et al. 1997). Thus, it is just as viable that the inner arm is trailing, rather than leading.

Elmegreen & Block (1999) have discussed more sophisticated models of dust, which include the effects of scattering. They note that, when the inclination is high enough, the color change across the line of nodes along the minor axis can be almost steplike in $V-K$. They also argue that the reddening asymmetry seen in many galaxies is not due to a preferential dust screen on one side, but that dust is always present on both sides of the line of nodes. The fact that we can see such dust on and across to the far side of the line of nodes is a strong argument that the observed reddening asymmetry in NGC 4622 is due to tilt.

10.2. *The Influence of a Minor Merger*

As noted by the referee, there is surprisingly little evidence for disruption in NGC 4622, except for the odd winding of its three spiral arms. We nevertheless suspect that a minor merger (in the form of a plunging encounter that left some debris in the center) could be responsible for the unusual structure seen in NGC 4622. This idea is developed more fully in Paper II. Here we note that several characteristics support the idea that NGC 4622 has suffered at least one recent minor merger. The first characteristic is that the galaxy is slightly lopsided, with an $m = 1$ relative Fourier amplitude of about 25% just inside the standard isophotal radius (see Fig. 9 of BCB). Rix & Zaritsky (1995) have shown that 30% of field spirals in a magnitude-limited sample have significant $m = 1$ components in their stellar light distributions. Zaritsky & Rix (1997) have suggested that these components are largely caused by tidal interactions, and they estimate the merger rate of small companions. However, as noted by the referee, the lopsidedness alone may not be conclusive for NGC 4622, because Jog (2002) has shown that a lopsided halo potential can produce similar effects.

A more convincing detail that suggests a minor merger occurred in NGC 4622 is its short central dust lane. Unusual dust lanes are often characteristic of mergers, such as the dust lanes in Centaurus A (Sandage 1961), NGC 1316 (Schweizer 1980), and the Blackeye Galaxy, NGC 4826 (Braun et al. 1994, discussed further in the next section). The slight change in position angle of NGC 4622's central dust lane suggests that the feature is a warped accretion disk. A consequence of the plunging encounter that may have led to this feature is that the nucleus of NGC 4622 could have engaged in an oscillation that might have helped to trigger the galaxy's lopsidedness (see Miller & Smith 1992, 1994). In this regard, Elmegreen (2002, private communication) has suggested that perhaps the inner parts of NGC 4622 are oscillating with respect to the outer parts. A possible signature of an oscillating nucleus is a miscentering of isophotes near the center (Miller & Smith 1992). In NGC 4622 nuclear isophotes are fairly well-centered (see Fig. 9a of BCB), with significant asymmetry appearing only at the beginning of the inner single arm.

We do not suggest that the particular merger that led to the central dust lane in NGC 4622 is necessarily the one that led to the peculiar leading arms. For example, Byrd et al. (1993) focussed on a small companion galaxy, a likely dwarf E, lying 1.85 east (see Fig. 3 of BCB) as a possible perturber as well. Nevertheless, the central dust lane is a very unusual feature to see in a nearly face-on spiral galaxy. The mass of dust involved could help us to determine how significant the companion that plunged might have been relative to the mass of NGC 4622 itself.

10.3. *Other Examples of "Two-Way" Spiral Patterns*

It is important to emphasize that NGC 4622 is not unique. Other galaxies are known that show features in common with NGC 4622's spiral pattern. Here we discuss two other cases having inner single arms and two or more outer arms winding in opposite senses. We also discuss an unusual case of a galaxy having two inner arms and two or more outer arms winding in opposite senses.

10.3.1. *The Blackeye Galaxy, NGC 4826 (M64)*

The idea that a single inner arm trails and two outer arms lead is not unprecedented. Walterbos, Braun, & Kennicutt (1994) discuss the spiral structure of the Blackeye Galaxy, NGC 4826 (M64), a well-known case with counterrotating atomic and ionized gas disks (Braun et al. 1994). Van Driel & Buta (1993) had noted a similarity between NGC 4826 and NGC 4622, in that the inner spiral structure looks single-armed and winds in the opposite sense from two outer arms. Walterbos et al. (1994) used the dust silhouette method in conjunction with $H\alpha$ and stellar rotation curves to deduce that the inner spiral structure trails, while the two outer arms lead in NGC 4826. This assertion led to little controversy because the features seen in NGC 4826 are relatively weak compared with those seen in NGC 4622. Nevertheless, it would still be difficult to account even for two weak outer leading arms in conventional density wave theory. NGC 4826 is more abnormal looking than NGC 4622, in that it has much more significant near-side absorption, which gives it its name. It is very likely that an interaction has caused the peculiar structure of NGC 4826, because the galaxy shows counterrotation of its gas disks. The kinematics of atomic hydrogen in NGC 4622 have been mapped with ATCA in late 2002 and will be described in a separate paper (Ryder et al. 2003).

10.3.2. *A CSRG Galaxy*

In the Catalogue of Southern Ringed Galaxies (Buta 1995), the spiral galaxy ESO 297-27, type SA(rs)b, is noted to have possible two-way spiral structure, involving a single inner arm winding in the opposite sense to at least two outer spiral arms. This deduction, based on a small-scale image from the SRC-J southern sky survey, was not conclusive. However, recently Grouchy & Buta (2003) imaged the galaxy with a CCD and have been able to verify the oppositely winding patterns (see Fig. 35). The observations were made with the CTIO 1.5 m telescope in 2002 August, and images were obtained with B , V , I , and $H\alpha$ filters. The galaxy differs from NGC 4622 in that it has a later Hubble type, is inclined about 55° , has a disk filled with diffuse ionized gas, and the relative amplitudes of the spiral arms are such that the inner arm is stronger than the outer arms. We also can identify three outer arms. Like NGC 4622, at least one set of arms in

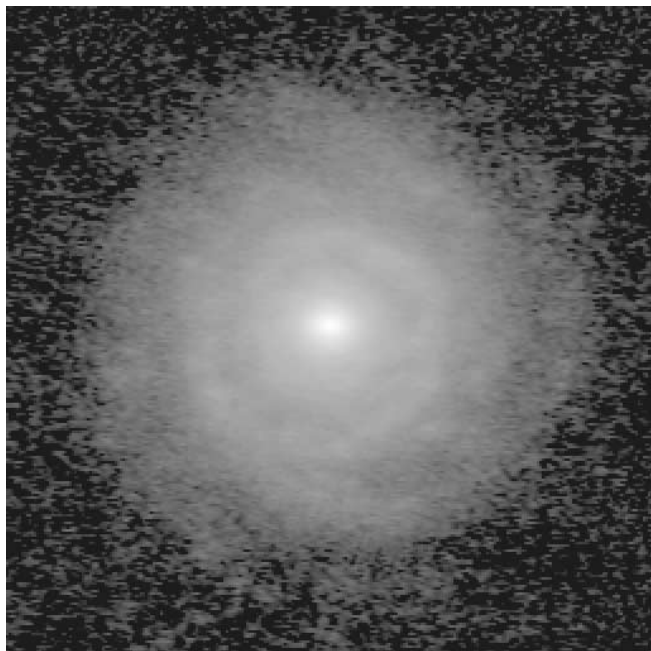


FIG. 35.—Ground-based CCD image (sum of B -, V -, and I -band images) of ESO 297-27, a newly identified “two-way” spiral (Grouchy & Buta 2003). The image has been deprojected from a 55° assumed inclination to better display the galaxy’s structure. In this case a single inner arm opens outward clockwise, while up to three weaker outer arms open outward counterclockwise. The field shown is 1.89 square arcseconds. Field stars have been removed.

ESO 297-27 must be leading; but, unlike NGC 4622, the more favorable geometry means that a more conclusive test can be made as to which arms lead. More information and follow-up data on this intriguing system will be provided in Grouchy & Buta (2003).

10.3.3. *The Ringed Spiral Galaxy NGC 3124*

This nearly face-on barred spiral galaxy, type SAB(rs)bc (de Vaucouleurs et al. 1991), shows an oppositely winding spiral pattern in a red continuum image obtained by Purcell (1998). Buta (1999) presents an $m = 2$ Fourier image in the I -band, which shows that the apparent bar of NGC 3124 can be thought of as a very open two-armed spiral pattern winding in the opposite sense to a more tightly wound multi-armed outer spiral pattern. Like NGC 4622, an inner ring marks the boundary between the domains of the opposing spirals. The low inclination of NGC 3124 and its relatively small bulge have not yet allowed a conclusive determination of which arms lead. Nevertheless, NGC 3124 provides an intriguing case of a two-way spiral that, like NGC 4622, seems to involve a ring as the boundary between the domains of the two opposing sets of arms.

10.4. *The Location of Resonances and the Inner Ring of NGC 4622*

The nature of rings in nonbarred galaxies is in general poorly understood. Nonbarred galaxies are less likely to have rings than barred galaxies (e.g., Buta 1995), but ringed nonbarred galaxies are nevertheless frequent enough to be significant. Some nonbarred ringed galaxies are likely to be “ex-barred” galaxies or galaxies with strong ovals (Buta 1999), but cases such as NGC 4622 clearly do not fit into this

category. In several cases (e.g., NGC 7742, de Zeeuw et al. 2002; NGC 4138, Jore, Broeils, & Haynes 1996) the ring is counterrotating with respect to the main stellar disk.

The inner ring of NGC 4622 is a remarkably complex feature. BCB noted the offset of the center of the ring from the nucleus of the galaxy. The lack of any obvious barlike distortion suggests that this ring has an unusual origin compared with most rings seen in barred or weakly barred galaxies. Based on the study of Byrd et al. (1993), Buta (1999) suggested that the ring in NGC 4622 is a tidally driven feature, rather than a bar-driven one. Byrd et al. (1993) suggested that a plunging retrograde encounter could account for both the mostly stellar inner single arm and the two outer gaseous arms. However, in their model the two outer arms are trailing material arms. BCB suggested that the ring is a $+1:1$ resonance with the angular velocity of a companion at closest approach. However, if the two outer arms are leading, the nature of the ring becomes more mysterious. Why does it delineate the boundary between the two opposing senses of spiral structure? If it is a resonance feature, which resonance might it be?

Elmegreen, Elmegreen, & Seiden (1989) have examined smooth spiral arm amplitude variations in three grand-design spirals (M51, M81, and M100) and have interpreted the minima in terms of the interference between inward and outward propagating spiral density waves. When they link prominent Fourier amplitude minima in each of these spirals to the inner $4:1$ resonance, they find that the outer spirals terminate near the outer Lindblad resonance. In Figure 9*b* of BCB and also in Figure 11*b* in this paper the relative $m = 2$ Fourier amplitude in the outer spiral arms of NGC 4622 shows a minimum at $r \approx 40''$. If this minimum corresponds to the inner $4:1$ resonance, then we can infer the locations of other resonances. From a fit of a quadratic to the observed folded rotation curve (Table 2), this resonance identification implies an inner Lindblad resonance at $r = 21''$, consistent with the average radius of the inner ring. However, the rising rotation curve leaves corotation indeterminate, although this resonance would clearly be beyond the outer boundary of the outer spiral arms if the $4:1$ resonant interpretation of the minimum is correct.

Another way to locate corotation in a grand-design spiral was proposed by Puerari & Dottori (1997; see also Vera-Villamizar et al. 2001). This method uses blue and near-infrared images to look for a phase shift of star formation relative to a spiral density wave that is expected to occur across the corotation resonance. In NGC 4622 we see phase shifts of the type that they predict in the boundary between the inner single arm and the two outer arms, and in the middle of the outer arms. Figure 36 shows enlargements of the $m = 2$ phases around these regions. Figure 36*a* shows that a strong B to I phase shift occurs at $r = 21''.4$. This is also where a large phase shift occurs in the $m = 1$ component in Figure 11*a*. When we plot this radius on a deprojected image of the galaxy (see Fig. 37), we find that it coincides with the zone where the inner single arm meets the inner ring; the radius represents a natural division between the inner and outer spirals in NGC 4622. In the outer arms (Fig. 36*b*) a much smaller phase shift occurs in the opposite sense at $r = 36''.4$. This radius is shown as the larger circle in Figure 37, and it passes between regions 1 and 2 shown in Figure 33. Comparing the plots with Figure 2 of Puerari & Dottori (1997), we find that the phase change in the outer arms, although very small, is consistent with a two-armed leading

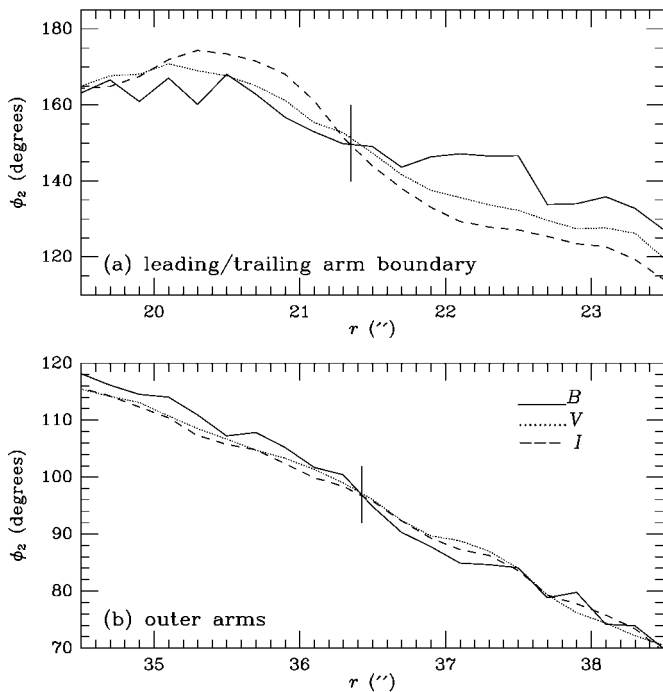


FIG. 36.—Enlargements of the behavior of the phase of the $m = 2$ component of NGC 4622 around two likely significant radii. (a) Region of the transition from the single inner arm to the two outer arms, and (b) region in the outer arms where star formation changes from being on the convex side of the arms to the concave side.

pattern (as noted already in § 10.1). However, the small size of the phase shift, as well as the rising rotation curve, complicates this interpretation. Nevertheless, on the northeast side, where the star formation differences are most obvious, the observed rotation curve still favors a slightly declining angular velocity, which might be enough to cause the observed phase shift.

Referring again to Figure 2 of Puerari & Dottori (1997), the much larger phase change in Figure 36a is at first sight consistent with the inner arm also being leading. However, the applicability of the Puerari & Dottori method to this zone is unclear, since their method assumes the presence only of a single two-armed density wave winding either clockwise or counterclockwise, not nested, oppositely winding patterns. The two outer arms intersect the inner arm roughly north and south of the nucleus, and since these arms are bluer than the inner arm, they impact the Fourier phases in the transition zone.

These results do not really clarify the nature of the inner ring. We believe this can best be answered only with a detailed dynamical model of the galaxy. In Paper II we will interpret the phase change at $r = 21''.4$ as a corotation radius for a pair of $m = 1$ periodic orbits in the form of two nested ellipses with maximum radii 180° apart. While Paper II will create the arm structure via a plunging encounter, the central regions will evolve toward the survival for such periodic orbits.

11. CONCLUSIONS

Our main conclusions from this study are as follows:

1. The two strong outer spiral arms in NGC 4622 appear to have the leading sense. This is based on the standard dust

silhouette method in conjunction with radial velocities used to infer spiral arm winding sense in the much earlier studies of Hubble (1943) and de Vaucouleurs (1958). In this paper, the principal evidence for this conclusion is based on the observed velocity field in Figure 13, the $V-I$ color index map in Figure 16, and the residual intensity map in Figure 17.

2. Isophote shapes suggest an inclination of 26° . However, the $H\alpha$ kinematics as well as the 21 cm line profile width favor a lower inclination, closer to 20° .

3. NGC 4622 has a significant bulge component, which allows the dust silhouette method to be used reliably even if the galaxy's inclination is only about 20° . The reddening asymmetry across the line of nodes is so obvious that it almost argues for the higher inclination to be correct.

4. There is clear reddening on both sides of the line of nodes, so there is no need to assume that the reddening asymmetry seen in the galaxy is purely intrinsic and has nothing to do with tilt. We see the expected effect that far-side dust lanes are muted compared with near-side lanes.

5. A model of the dust distribution in a tilted symmetric galaxy was used to show the feasibility of detecting, at *HST* resolution, a near side–far side reddening asymmetry to an inclination as low as 15° , given the observed bulge and disk parameters of NGC 4622. Observed asymmetry curves along the kinematic major and minor axes show some of the expected effects but are complicated by details along each axis.

6. The distribution of star formation in the outer arms weakly supports the leading sense of the arms, based on the Puerari & Dottori (1997) method of locating corotation. The effect found (a phase shift in the location of star-forming regions relative to the background stellar arms) is small, but is at least consistent with the dust asymmetry results. The reliability of the method, however, is questionable in the presence of a rising rotation curve. Nevertheless, the observed rotation curve on the northeast side still favors a slightly declining angular velocity with radius, which may be enough allow the phase shift to be seen.

7. Toomre has argued independently that the small-scale aspects of the dust lanes on the east side of the inner ring strongly favor a counterclockwise rotation and trailing sense for the outer arms. However, this does not explain why the reddening asymmetry appears to know the line of nodes, nor does it account for the inner single spiral arm.

8. The ionized gas in NGC 4622 mainly follows the two outer stellar arms and the southwest portion of the inner ring. Thus, it is unlikely that these gaseous arms represent a separate system counterrotating relative to the stars, as is sometimes observed in other galaxies. The observed kinematics of the $H\ II$ regions is such that the rotation curve is rising across the outer arms. This rise is not an artifact of streaming motions. In contrast to the ionized gas, the near-infrared light distribution predicts, under the assumption of a constant mass-to-light ratio, a normal relatively flat rotation curve. The implication is that NGC 4622 may be dark matter-dominated even in the inner parts of the visible disk.

9. NGC 4622 has a significant system of old globular clusters that extends well beyond the main optical region. The specific frequency of this system is 3.4 ± 0.6 , and its mean color is $\langle (V-I)_0 \rangle = 1.04 \pm 0.19$. The inferred turnover in the globular cluster luminosity function confirms the membership of the galaxy in the Centaurus Cluster.

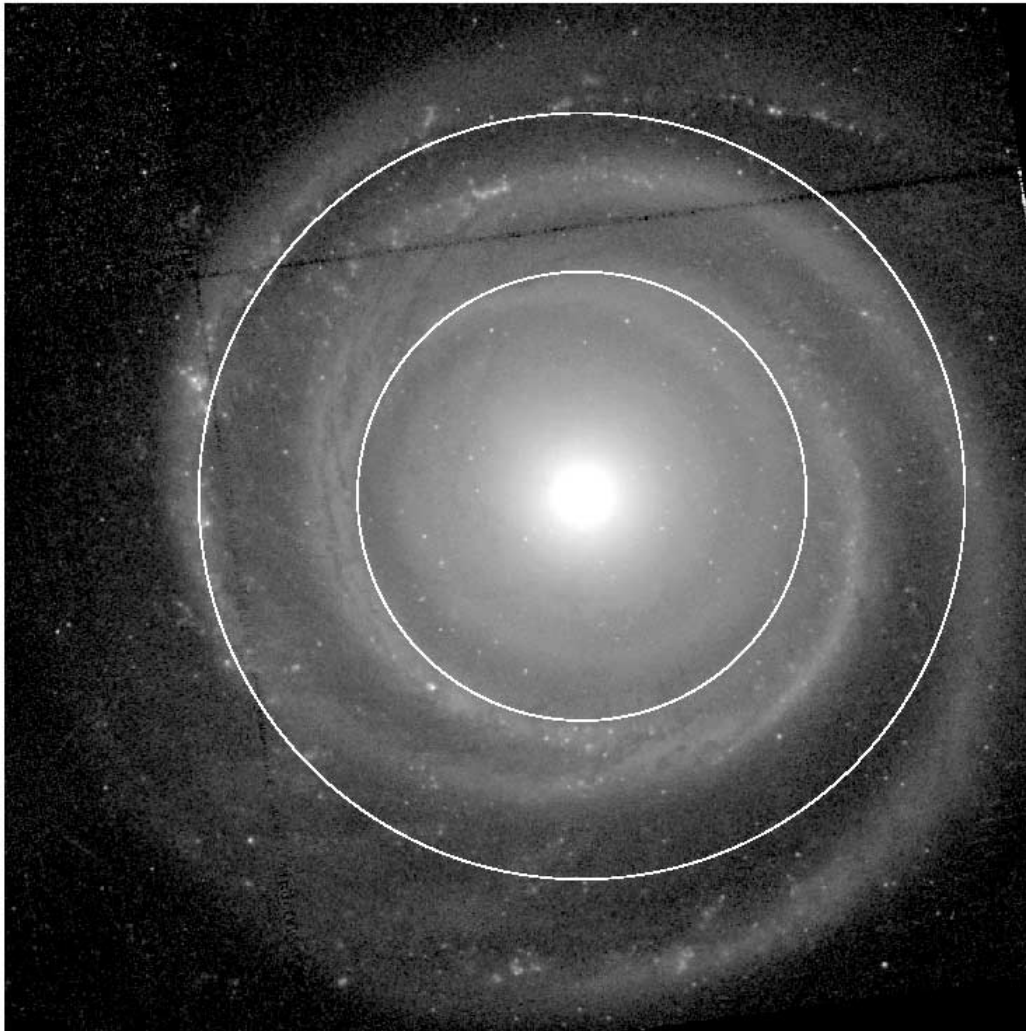


FIG. 37.—Deprojected V -band WFC2 image showing the locations of the transition radii highlighted in Fig. 36. The field covers a region $1'.63 \times 1'.63$ in area, and is oriented such that the kinematic line of nodes is vertical.

10. NGC 4622 is not unique as a “two-way” spiral. At least three other examples are known. These include, NGC 4826, where two weak outer arms have been suggested to be leading; ESO 297-27, which shows a bright single inner arm winding opposite to three weaker outer arms; and NGC 3124, an inner-ringed spiral where a barlike feature can be interpreted as an open two-armed spiral winding opposite to the outer arms. These cases suggest that leading spirals may not be as rare or impossible as once thought. More examples will no doubt be found as awareness of the phenomenon becomes greater.

Further studies of NGC 4622 are needed to better assess exactly what is going on, particularly observations of its stellar and atomic gas kinematics. If the galaxy has an extended H I disk, this may provide information on possible warping. The galaxy also needs to be checked for counter-rotation in the inner regions, an aspect that may be common among early-type disk galaxies. Haynes et al. (2000) describe kinematic studies of four early-type galaxies and find evidence in each case for a decoupling of the ionized gas and stellar disks, sometimes throughout the disk or in the central area. Minor mergers are likely to be responsible for these unusual components. In NGC 4622 we have used the

stellar light distribution to assess the near side and the ionized gas to assess the kinematics. If the ionized gas disk is coupled to the stellar disk morphologically, as it appears to be in NGC 4622 (that is, the ionized clouds for the most part follow the stellar arms), then this should be a fair way to determine the sense of winding of the spiral arms in NGC 4622.

Table 3 provides a summary of all of the main parameters of NGC 4622 derived in this paper.

We thank M. Meyer and S. D. Ryder for getting us a 21 cm line profile of NGC 4622 on short notice, and especially M. Meyer for deriving some of the parameters of the profile. We also thank Z. Levay and the Hubble Heritage Team for making the fine color image of NGC 4622, which we use in Figure 1 of this paper. We acknowledge helpful comments from A. Toomre, B. G. Elmegreen, and especially from an anonymous referee. This work was supported by NASA/STScI grant GO 8707 to the University of Alabama and NSF grant 9802918 to Beville State College in Fayette. This research has made use of the NASA/IPAC Extragalactic Database, which is operated by the Jet Propulsion Laboratory, California Institute of Technology, under contract

TABLE 3
SUMMARY OF DERIVED PARAMETERS OF NGC 4622

Parameter	Value
Distance assumed.....	40.2 ± 3.1 Mpc (Tully & Pierce 2000)
GCLF distance	44.6 ± 3.7 Mpc (this paper)
Photometric inclination	26° ± 4°
Optical systemic velocity	4502 ± 3 km s ⁻¹
Kinematic inclination ^a	19°3 ± 1°7
Bulge effective radius.....	9''38 ± 0''56
Disk effective radius	26''0 ± 0''2
$B(0)_c$ (Freeman 1970)	21.81 mag arcsec ⁻²
Total magnitude B_T	13.44
Total magnitude I_T	11.09
Total magnitude H_T	9.16
Absolute magnitude $M_B^{b,k,l}$	-20.3
Relative bulge luminosity $k_1(B)$	0.39
Relative bulge luminosity $k_1(I)$	0.51
Relative bulge luminosity $k_1(H)$	0.58
GC specific frequency.....	3.4 ± 0.6
GC $\langle(V-I)_0\rangle$	1.04 ± 0.19

^a Based on observed 21 cm line width and assumed distance of 40.2 Mpc (see text).

with the National Aeronautics and Space Administration. The Digitized Sky Surveys were produced at the STScI under grant NAG W-2166. The images of these surveys are based on photographic data obtained using the Oschin Schmidt Telescope on Palomar Mountain and the UK Schmidt Telescope. The plates were processed into the present compressed digital form with the permission of these institutions. Funding for the OSU Bright Spiral Galaxy Survey was provided by grants from the NSF (grants AST 92-17716 and AST 96-17006), with additional funding by Ohio State University.

APPENDIX A

MODEL OF THE NEAR SIDE-FAR SIDE REDDENING ASYMMETRY IN A LOW-INCLINATION GALAXY

For the disk component, we use a double exponential having volume luminosity density ($L_\odot \text{pc}^{-3}$)

$$E^{\text{II}}(R, z) = E_0^{\text{II}} e^{-R/h_R} e^{-z/h_z},$$

where h_R is the radial scale length and h_z is the vertical scale height. For the bulge component, we use the Young (1976) asymptotic volume density for the $r^{1/4}$ law for a spherical galaxy:

$$E^{\text{I}}(r) = E_0^{\text{I}} \frac{e^{-bj}}{2j^3} \left(\frac{\pi}{8bj} \right)^{1/2},$$

where $j = (r/r_e)^{1/4}$ and b is a constant, 7.669. Here r_e is the effective radius of the bulge in projection. The parameters h_R , r_e , E_0^{I} , and E_0^{II} are based on the bulge/disk decompositions. The parameter h_z is assumed to be 325 pc, the same as for the Galaxy (Gilmore & Reid 1983).

In our model galaxy, we assume there is a dust layer having vertical half-thickness $h_d = 0.3h_z$. There are two parts to

this dust layer. The extended part is a uniform layer having face-on optical depth $\tau_{0d}(V) = 0.3$ and $\tau_{0d}(I) = 0.18$. Within this layer there are four rings each having a width of 12 pixels (= 0''12) centered at radii of 1''0, 2''0, 4''0, and 6''0. Each ring is assumed to have $\tau_{0r} = 3\tau_{0d}$. (These optical depths are based roughly on the analysis of overlapping galaxy pairs by White & Keel 1992). With these features, we integrate the bulge and disk light in three parts each: the part in front of the dust layer, the part mixed with the dust layer, and the part behind the dust layer. For a line of sight passing through coordinates (x_0, y_0) in the disk plane, the cylindrical radius for a point at z relative to the plane is $R(z) = [(x_0^2 + (y_0 + z \tan i)^2)]^{1/2}$, where i is the assumed inclination. Then the three contributions for the disk component are given by

$$\begin{aligned} I^{\text{II}}(x_0, y_0) = & \int_{h_d}^{\infty} E^{\text{II}}(R(z), z) \sec i \, dz \\ & + \int_{-h_d}^{h_d} E^{\text{II}}(R(z), z) \sec i \\ & \quad \times e^{-[\tau_0(h_d-z) \sec i]/2h_d} \, dz \\ & + \int_{-\infty}^{-h_d} E^{\text{II}}(R(z), z) (\sec i) e^{-\tau_0 \sec i} \, dz. \end{aligned}$$

For the bulge component surface brightness at (x_0, y_0) , we use the radius $r = [(x_0^2 + (y_0 + z \tan i)^2 + z^2)]^{1/2}$. Then the three contributions for the bulge component are given by

$$\begin{aligned} I^{\text{I}}(x_0, y_0) = & \int_{h_d}^{\infty} E^{\text{I}}(r(z)) \sec i \, dz \\ & + \int_{-h_d}^{h_d} E^{\text{I}}(r(z)) (\sec i) e^{-[\tau_0(h_d-z) \sec i]/2h_d} \, dz \\ & + \int_{-\infty}^{-h_d} E^{\text{I}}(r(z)) (\sec i) e^{-\tau_0 \sec i} \, dz. \end{aligned}$$

The final model involves summing the contributions for the bulge and disk components in both V and I , matching the resolution by smoothing each model image with a Gaussian whose full width at half maximum is consistent with the stars on the original images, and then adding noise consistent with the observed images.

APPENDIX B

DISCOVERY OF A SUPERNOVA IN THE WFPC2 IMAGES

The WFPC2 images we have used in this paper, which were taken from 2001 May 25.57–25.91 UT, reveal a likely supernova located 91''9 slightly east of north of the nucleus (see Fig. 38). The object is seen on all four filters used for our WFPC2 exposures. The coordinates of the object are R.A. (J2000.0) = 12^h42^m40^s.04, decl. (J2000.0) = -40°43'12''54. There is nothing at this position in the field of the galaxy seen on the Digitized Sky Survey. At the adopted distance of 40.2 Mpc, this position projects 18 kpc from the nucleus, well outside the visible disk. Since there is no evidence of any massive star formation in this region, it is possible that the object is a Type Ia supernova. Its

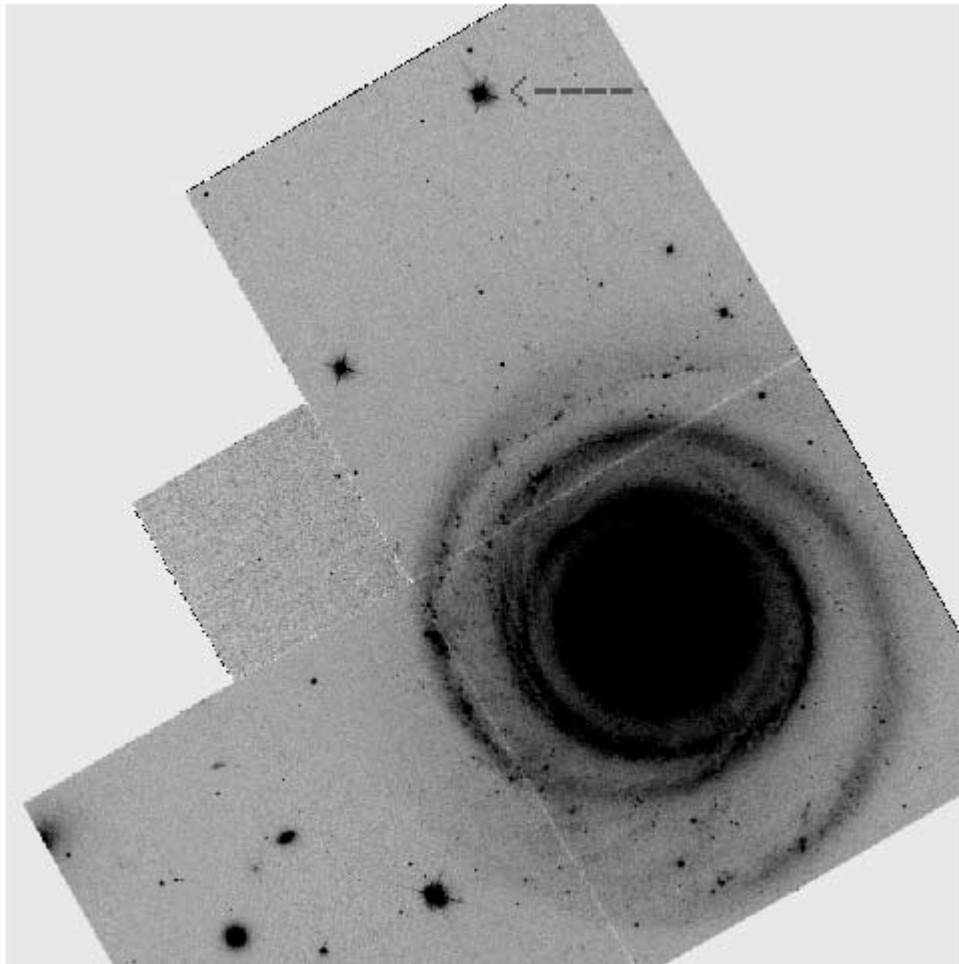


Fig. 38.—*HST* WFPC2 F555W image of NGC 4622, rotated so that north is at the top, and east to the left. The arrow points to a supernova, now known as SN 2001jx (Buta et al. 2002), which was present during the WFPC2 observations. The arrow has a length of $21''5$.

location so far from the center prevented it from being noticed when the images were first obtained. The object has been designated SN 2001jx by the IAU Central Bureau of Astronomical Telegrams (Buta, Byrd, & Freeman 2002).

The image of the possible supernova is saturated on all but the F336W image, which gives $U = 17.5$ (May 25.6

UT). The apparent $U-B$ color index is $+0.3$ or greater. After correcting for Galactic extinction and referring to the U -band light curve of SN 1981b in NGC 4536 (Buta & Turner 1983), we estimate that our images were taken about 15–20 days past maximum light if the object is a Type Ia supernova.

REFERENCES

- Athanassoula, E. 1978, *A&A*, 69, 395
 Binney, J., & Tremaine, S. 1987, *Galactic Dynamics* (Princeton: Princeton Univ. Press)
 Braun, R., Waltherbos, R. M., Kennicutt, R. C., & Tacconi, L. J. 1994, *ApJ*, 420, 558
 Bridges, T. J., & Hanes, D. A. 1992, *AJ*, 103, 800
 Bruzual, G., & Charlot, S. 1996, in *AAS CD-ROM Series*, Vol. 7
 Buta, R. 1995, *ApJS*, 96, 39
 ———. 1999, *Ap&SS*, 269, 79
 Buta, R., Byrd, G. G., & Freeman, T. 2002, *IAU Circ.* 7833
 Buta, R., & Combes, F. 1996, *Fundam. Cosmic Phys.*, 17, 95
 Buta, R., Crocker, D. A., & Byrd, G. G. 1992, *AJ*, 103, 1526 (BCB)
 Buta, R., & Purcell, G. B. 1998, *AJ*, 115, 484
 Buta, R., & Turner, A. 1983, *PASP*, 95, 72
 Buta, R., Treuthardt, P. M., Byrd, G. G., & Crocker, D. A. 2000, *AJ*, 120, 1289
 Byrd, G., Freeman, T., & Buta, R. 2003, in preparation (Paper II)
 Byrd, G., Freeman, T., & Howard, S. 1993, *AJ*, 105, 477
 ———. 1994, *AJ*, 108, 2078
 Byrd, G. G., Purcell, G. B., Buta, R. J., McCormick, D., & Freeman, T. 1997, in *AIP Conf. Ser.* 393, *Star Formation Near and Far*, ed. S. S. Holt & L. G. Mundy (Melville, NY: AIP), 283
 Byrd, G. G., Thomasson, M., Donner, K. J., Sundelius, B., Huang, T.-Y., & Valtonen, M. J. 1989, *Celest. Mech.*, 45, 31
 Carollo, C. M., Stiavelli, M., & Mack, J. 1998, *AJ*, 116, 68
 Carollo, C. M., Stiavelli, M., Seigar, M., de Zeeuw, P. T., & Dejonghe, H. 2002, *AJ*, 123, 159
 de Vaucouleurs, G. 1958, *ApJ*, 127, 487
 de Vaucouleurs, G., de Vaucouleurs, A., Corwin, H., Buta, R., Paturel, G., & Fouqué, P. 1991, *Third Reference Catalogue of Bright Galaxies* (New York: Springer) (RC3)
 de Zeeuw, P. T., et al. 2002, *MNRAS*, 329, 513
 Elmegreen, B. G., & Block, D. L. 1999, *MNRAS*, 303, 133
 Elmegreen, B. G., Elmegreen, D. M., & Seiden, P. E. 1989, *ApJ*, 343, 602
 Eskridge, P., et al. 2000, *AJ*, 119, 536
 Faber, S. M., et al. 1997, *AJ*, 114, 1771
 Freeman, K. C. 1970, *ApJ*, 160, 811
 Garcia, A. M. 1993, *A&AS*, 100, 47
 Gilmore, G., & Reid, N. 1983, *MNRAS*, 202, 1025
 Grillmair, C., Faber, S. M., Lauer, T. R., Hester, J. J., Lynds, C. R., O'Neill, E. J., & Scowen, P. A. 1997, *AJ*, 113, 225
 Grouchy, R., & Buta, R. 2003, in preparation
 Harris, W. E., Harris, H. C., & Harris, G. L. H. 1984, *AJ*, 89, 216
 Harris, W. E., & van den Bergh, S. 1981, *AJ*, 86, 1627
 Haynes, M. P., Jore, K. P., Barrett, E. A., Broeils, A. H., & Murray, B. M. 2000, *AJ*, 120, 703
 Holtzman, J. A., Burrows, C. J., Casertano, S., Hester, J. J., Trauger, J. T., & Watson, A. M., & Worthey, G. 1995, *PASP*, 107, 1065

- Hubble, E. 1943, *ApJ*, 97, 112
 Jedrzejewski, R. 1987, *MNRAS*, 226, 747
 Jog, C. J. 2002, *A&A*, 391, 471
 Jore, K. P., Broeils, A. H., & Haynes, M. P. 1996, *AJ*, 112, 438
 Joyce, R. R. 1992, in *ASP Conf. Ser. 23, Astronomical CCD Observing and Reduction Techniques*, ed. S. B. Howell (San Francisco: ASP), 258
 Julian, W. H., & Toomre, A. 1966, *ApJ*, 146, 810
 Kent, S. M. 1986, *AJ*, 91, 1301
 ———. 1988, *AJ*, 96, 514
 Kissler-Patig, M., Kohle, S., Hilker, M., Richtler, T., Infante, L., & Quintana, H. 1997, *A&A*, 319, 470
 Kormendy, J. 1987, in *IAU Symp. 127, Structure and Dynamics of Elliptical Galaxies*, ed. T. de Zeeuw (Dordrecht: Reidel), 17
 Kundu, A., & Whitmore, B. C. 2001, *AJ*, 122, 1251
 Larsen, S. S., Forbes, D. A., & Brodie, J. P. 2001, *MNRAS*, 327, 1116
 Lauer, T., et al. 1995, *AJ*, 110, 2622
 Lucey, J. R., Currie, M. J., & Dickens, R. J. 1986, *MNRAS*, 221, 453
 McGlynn, T. A. 2002, *SkyView: The Internet's Virtual Telescope*
 Miller, R. H., & Smith, B. F. 1992, *ApJ*, 393, 508
 ———. 1994, *Cel. Mech. Dyn. Astron.*, 59, 161
 Mollenhoff, C., & Heidt, J. 2001, *A&A*, 368, 16
 Puerari, I., & Dottori, H. 1997, *ApJ*, 476, L73
 Purcell, G. B. 1998, Ph.D. thesis, Univ. Alabama
 Quillen, A. C., Frogel, J. A., & González, R. A. 1994, *ApJ*, 437, 162
 Rix, H.-W., & Zaritsky, D. 1995, *ApJ*, 447, 82
 Rogstad, D. H. 1971, *A&A*, 13, 108
 Rubin, V. C., Burstein, D., Ford, W. K., & Thonnard, N. 1985, *ApJ*, 289, 81
 Ryder, S. D., Meyer, M., Grouchy, R., & Buta, R. 2003, in preparation
 Sandage, A. 1961, *The Hubble Atlas of Galaxies* (Washington: Carnegie Inst. Washington)
 Schlegel, D. J., Finkbeiner, D. P., & Davis, M. 1998, *ApJ*, 500, 525
 Schommer, R. A., Bothun, G. D., Williams, T. B., & Mould, J. R. 1993, *AJ*, 105, 97
 Schweizer, F. 1976, *ApJS*, 31, 313
 ———. 1980, *ApJ*, 237, 303
 Scott, J. S. 1996, Master's thesis, Univ. Alabama
 Sérsic, J. 1968, *Atlas de Galaxias Australes* (Córdoba: Obs. Astron., Univ. Nac. Córdoba)
 Simien, F., & de Vaucouleurs, G. 1986, *ApJ*, 302, 564
 Tonry, J. L., Dressler, A., Blakeslee, J. P., Ajhar, E. A., Fletcher, A. B., Luppino, G. A., Metzger, M. R., & Moore, C. B. 2001, *ApJ*, 546, 681
 Toomre, A. 1981, in *The Structure and Evolution of Normal Galaxies*, ed. S. M. Fall & D. Lynden-Bell (Cambridge: Cambridge Univ. Press), 111
 Tully, R. B., & Pierce, M. J. 2000, *ApJ*, 533, 744
 Vera-Villamizar, N., Dottori, H., Puerari, I., & de Carvalho, R. 2001, *ApJ*, 547, 187
 Walterbos, R. A. M., Braun, R., & Kennicutt, R. C. 1994, *AJ*, 107, 184
 Warner, P. J., Wright, M. C. H., & Baldwin, J. E. 1973, *MNRAS*, 163, 163
 White, R. E., & Keel, W. C. 1992, *Nature*, 359, 129
 Whitmore, B., Heyer, I., & Casertano, S. 1999, *PASP*, 111, 1559
 Worthey, G. 1994, *ApJS*, 95, 107
 van Driel, W., & Buta, R. 1993, *PASJ*, 45, L47
 Young, P. J. 1976, *AJ*, 81, 807
 Zaritsky, D., & Rix, H.-W. 1997, *ApJ*, 477, 118